R83-956181F

Investigation of the Feasibility of Temperature Profiling Optical Diagnostics in the SSME Fuel Pre-Burner

Final Technical Report
Contract NAS8-34774

J. A. Shirley

June 1983

Prepared for
George C. Marshall Space Flight Center
Marshall Space Flight Center, Alabama 35812

United Technologies Research Center
East Hartford, Connecticut 06108

Investigation of the Feasibility of Temperature Profiling Optical Diagnostics in the SSME Fuel Pre-Burner

TABLE OF CONTENTS

R83-956181F

Investigation of the Feasibility of Temperature Profiling Optical Diagnostics in the SSME Fuel Pre-Burner

SUMMARY

Results of an analytical investigation performed by United Technologies Research Center (UTRC) under Contract NAS8-34744, sponsored by the George C. Marshall Space Flight Center to determine the feasibility of temperature profiling in the space shuttle main engine (SSME) fuel pre-burner are presented. In this application it is desirable to measure temperature in the pre-burner combustor with a remote, non-intrusive optical technique. Several techniques using laser excitation have been examined with a consideration of the constraints imposed by optical access in the fuel pre-burner and the problems associated with operation near the functioning space shuttle engine. The potential performance of practical diagnostic systems based on spontaneous Raman backscattering, laser-induced fluorescence, and coherent anti-Stokes Raman spectroscopy have been compared analytically. A system using collection of spontaneous Raman back-scattering excited by a remotely-located 5-10 Watt laser propagated to the SSME through a small diameter optical fiber was selected as the best approach. Difficulties normally associated with Raman scattering: weak signal strength and interference due to background radiation are not expected to be problematic due to the very high density in this application, and the low flame luminosity expected in the fuel-rich hydrogen-oxygen flame. The components of a Raman system have been examined critically and the limitations, if any, that they impose have been considered. Theoretical estimates of the performance of the Raman system indicate that it should be capable of achieving system design goals with respect to spatial, temporal, and temperature resolution with minor tradeoffs in overall performance.

INTRODUCTION

The Space Shuttle Main Engine (SSME) is one of the most critical components of probably the most ambitious engineering endeavor of the past decade. At full power it develops 512,000 lbs of thrust, and can be throttled from 65 percent of the 470,000 lbs of rated thrust to 109 percent. The SSME is designed for a life of 7.5 hrs with 55 starts, with some servicing of line replaceable units. Major technical hurdles have had to be overcome to develop this engine. Early in the development of the engine, problems were experienced with the failure of bearings in the oxidizer turbopump. Turbine blade life has been an area of concern and is the subject of an on-going upgrade of engine performance in terms of extending the usable life. This report indirectly addresses this problem. Turbine blade life is thought to be limited by fatigue possibly caused by nonuniform temperature profiles in the pre-burner. The development of modifications leading to more uniform temperature profiles would be greatly facilitated by a diagnostic capable of measuring temperatures in the engine. The objective of the investigation reported herein is to determine the best optical techniques for temperature profiling in the SSME pre-burner, and to determine on theoretical grounds the probability of success.

Optical diagnostics have been under development since the advent of high power and tunable lasers. A number of techniques have evolved to make measurements in a wide variety of combustion systems, including such practical environments as combustion research tunnels, internal combustion engines, large industrial furnaces and after-burning jet engine exhausts. Special, difficult problems are encountered in the environment of the SSME. These include: engine motion; fog, mist and ice formation near and on the engine; and severe vibration and acoustic noise levels in the vicinity of the engine. Optical measurements are also hampered by existing optical access into the pre-burner. Several optical techniques have been examined in light of these restrictions. These are laser-induced fluorescence, spontaneous Raman, and coherent nonlinear techniques, such as coherent anti-Stokes Raman spectroscopy (CARS). The potential performance of these optical techniques has been predicted and compared, based on properties of the flow in the pre-burner combustor and theoretical predictions and experience in optical combustion diagnostics.

Spontaneous Raman scattering has been selected as the best available technique based on the restrictions posed by the geometry and environment of the SSME pre-burner and the predicted favorable performance of Raman diagnostics. Spontaneous Raman requires only single port access, is capable of adequate performance in terms of program goals, and is amenable to implementation in an optical fiber configuration. This latter point is very important because the severe environment of the SSME engine dictates taking steps to maintain measurement integrity. An optical fiber should be insensitive to engine motion,

condensation on and around the engine, and the noise and vibration levels near the engine. Coherent optical techniques would be capable of measurements only along a line joining the two existing access ports in the combustor. Fluorescence measurements are not favorable due to a lack of adequate concentrations of species that are amenable to laser excitation. The introduction of a seed species is problematic and the existence of other usable techniques argues against this mode of operation.

The theory of Raman measurements in hydrogen, the major constituent in the SSME pre-burner post combustion flow, has been examined and the system elements comprising the diagnostics have been identified. In particular the use of optical fibers in this application has been closely studied. The levels of performance predicted considering practical system limitations compare favorably with the design performance criteria established by NASA. Problems which have not been studied are those which cannot be effectively studied on theoretical grounds alone. In particular, one potential problem which may hamper optical diagnostics is associated with the transmission of laser beams through the SSME pre-burner due to possible severe combustion turbulence or two-phase flow problems. In this regard the selected technique appears to be the most reasonable approach.

The results of the feasibility study are described in the following sections of this report. The next section describes the relevant optical techniques for SSME pre-burner optical diagnostics. The section opens with a description of the fuel pre-burner especially as regards optical probing. Then the diagnostic techniques are described and the performance of each is compared. The next section focuses on the use of Raman scattering techniques. The section starts with a review of the principles of Raman temperature measurements. The component parts of the Raman system are examined next. Particular attention is paid to the use of optical fibers in this section. Finally in this section, the performance of an optical diagnostic system based on Raman diagnostics is examined in the light of limitations of system elements just studied. Conclusions drawn from the study are then presented. References are contained in a separate section near the end of the report. Appendix A contains a compilation of Raman optical intensity calculations.

OPTICAL DIAGNOSTIC TECHNIQUES FOR TEMPERATURE MEASUREMENTS

This section describes the various optical diagnostic techniques available for temperature measurements in high pressure combustion. The SSME fuel pre-burner is described first, since its characteristics influence the choice of optical techniques. After this the optical diagnostic techniques most relevant to this application are introduced. The performance of these techniques is enumerated in the subsection following and the selection of best optical technique is justified.

The performance capability and the limitations of the selected technique, Raman backscattering is described in the section following this one.

Constraints on SSME Pre-Burner Optical Measurements

The fuel pre-burner reacts a large portion of the hydrogen flow with a small portion of the oxygen flow to provide a hot gas stream to drive the turbines that drive the fuel pump. The hot gas stream leaving the turbine is ducted to the main combustion chamber where it reacts with the remainder of the oxygen flow. The pre-burner operates very fuel-rich so the gas temperature in the turbopump is relatively low, approximately 970 K (1750 R) at the nominal power level.

Equilibrium calculations at the fuel pre-burner flow conditions at the nominal power level (NPL) indicate that molecular hydrogen is the dominant constituent in the combusted flow. Water vapor makes up the balance of the mixture at about 10 percent of the total flow. The atomic hydrogen, hydoxyl radical (OH), and hydrogen peroxide mole fractions are estimated to be very low. The calculated gas composition is shown in Table I.

TABLE I

FUEL PRE-BURNER CALCULATED COMPOSITION

NPL, p = 5500 psia

Species	Mole Fraction
H_2	0.89407
H_2O	0.10593
H	1.559×10^{-10}
OH	4.709×10^{-14}
H_2O_2, O_2, O, and O_3	$< 10^{-20}$

A cross section view of the fuel pre-burner is shown in Fig. 1. Fuel and oxidizer are introduced into the pre-burner chamber by injection (not shown) through the face plate. They react and exhaust to the turbine. Within the chamber are baffles and a liner, both of which are supplied with hydrogen flow for cooling. Transducer ports in the chamber walls permit optical access to the combustion medium. A special hole with a reinforcing bushing goes through the liner at the existing ports. There are only two existing transducer ports but two other ports could be added to bosses existing on the chamber. The ports are located at 60, 165, 210 and 300 degrees with respect to the fuel inlet. Therefore, there is no optical access directly across the pre-burner, that is line-of-sight through either the existing, or the additional ports. The baffle plates also restrict optical access as the axis of the transducer ports intersects the lower edge of the baffles. It is desirable, however, to restrict diagnostic systems to the use of these ports to avoid unnecessary penetrations through the chamber. These considerations favor single port techniques.

There are other problems associated with the challenging application of optical diagnostics in the environment of a large rocket engine. First, the SSME moves in the test stand, because the engine gimbals for thrust vector control and because the thrust load deflects the test stand slightly. These motions would preclude free transmission of a beam to the engine due the critical alignment usually required of optical components. Another factor that makes transmission of the laser beam to the engine difficult is the fact that prior to and during firing, the engine is surrounded by a vapor mist due to the condensation of atmospheric water by the cold cryogenic propellant lines. This mist would scatter a laser beam severely, thereby requiring the beam to be transported in a special tube purged with dry nitrogen, or an optical fiber. During firing and afterwards, frost forms on the engine and would be expected to form on attached components unless measures are taken to prevent it, such as by heating with warm nitrogen. Finally, very high vibration and noise levels are experienced at the engine, and somewhat lower levels prevail in instrumentation bays located in nearby hardened core of the engine test stand.

The optical properties of the flow within the pre-burner is unknown from an empirical point of view. From known flowrates it can be estimated that the Mach number is 0.005, so that compressibility effects are expected to be small. Nonuniformities in the refractive index resulting from incomplete combustion and possible two-phase flow may be problematic. The point of measurement is close to the point where coolant hydrogen is injected from the baffles. The magnitude of these possible problems can only be assessed in hot gas tests.

FIG. 1

ORIGINAL PAGE IS
OF POOR QUALITY

SSME PRE-BURNER CROSS SECTION

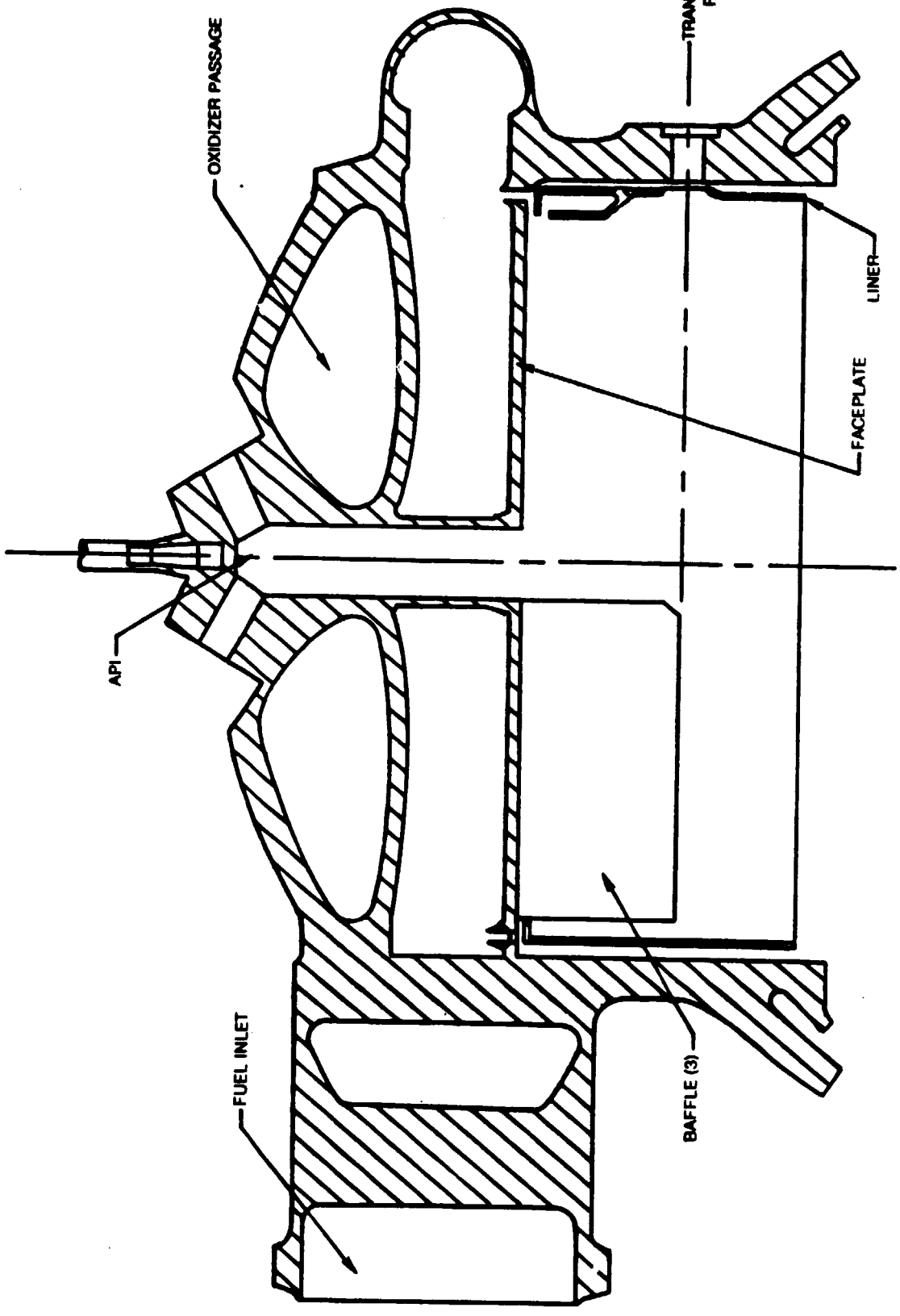

82-4-37-1

Optical Techniques for Temperature Measurements

The proliferation of high power and tunable lasers has encouraged the development of a number of optical methods for use in hostile flame environments (Refs. 1-3). Chief among the reasons for these developments is the desirability of non-perturbing measurement methods. The various optical techniques essentially probe individual excitation levels within the chemical species. The strengths of response of the various molecular levels can be related through analysis to populations in the flame from which the temperature can be deduced. A number of optical techniques have been developed. Among these spontaneous Raman, fluorescence and nonlinear optical techniques such as CARS and SRG have received the greatest attention recently for combustion applications. The advantages and disadvantages of these techniques for SSME pre-burner optical diagnostics are discussed in the following.

Fluorescence

Fluorescence (Refs. 1, 3, 4) is the emission of light from an atom or molecule promoted to an excited state. In laser fluorescence, the excitation takes place by the absorption of laser radiation tuned to coincide with a resonance in the probed species. The temperature is determined from an analysis of the distribution of spontaneous emission from the excited species. The hydroxyl radical is the only species existing in the pre-burner post flame gases at equilibrium (see Table I), which is amenable to probing by existing laser sources. OH has absorption bands between 2400 and 4000 Angstroms. Hydrogen and water vapor have optical absorption bands in the vacuum ultraviolet (Ref. 1), a region where few lasers are available and no windows can be used. However, the concentration of hydroxyl radical is very low due to the low combustion temperature and the fuel rich conditions in the pre-burner, making it a relatively poor choice as a probe species. Laser fluorescence is used to measure trace species; therefore, the use of this radical was investigated, and is reported in the next subsection.

The penalty imposed on fluorescence may be lifted by seeding the flow with a chemical substance which has good fluorescence properties. Seeding may be accomplished by mixing the compound with one of the propellants or by injecting it directly into the pre-burner. Both of these approaches presents problems. To mix the fluorescent species with the propellant requires that it be chemically inert with respect to the propellant and also that it be miscible with the cryogenic liquid phase. Injection would require a large number of injection ports in the injector face, which is not practical either.

Raman Scattering

Raman scattering (Refs. 5-7) is the process by which a molecule interacts inelastically with an incident photon, i.e., energy exchange between the molecules and photons occurs. If the molecule is initially in an unexcited state, the interaction leaves the molecule in an excited state and the scattered photon energy is lower than the incident photon energy by an amount corresponding to the molecular energy. Typically a number of internal energy levels can be excited, and they each scatter light at a characteristic frequency shift so that the temperature can be determined from the distribution of frequencies in the scattered radiation. Normally only a small number of molecules is excited in the scattering process so that no perturbation of the molecular populations occurs. The usual problem with Raman scattering for combustion diagnostics is that the scattering cross section is very small and the scattering is weak, so that background luminosity or laser-induced interferences may overwhelm the signal. Raman scattering also takes place into 4π steradians, so that usually only a fraction of the scattered light can be collected. Fortunately the SSME pre-burner is likely to have very low flame luminosity because a hydrogen flame emits very little radiation in the visible part of the spectrum. Furthermore, the high chamber pressure helps considerably to overcome the small Raman scattering cross section.

Nonlinear Optical Techniques

The emergence of high power lasers has promoted the development of several nonlinear optical techniques for combustion diagnostics. Chief among these are coherent anti-Stokes Raman spectroscopy (CARS) (Refs. 8-10) and stimulated Raman gain (SRG) (Ref. 11). The advantage of CARS and indeed all nonlinear techniques, which are coherent, is that signal radiation is generated or contained in a highly collimated beam which can be easily collected. Furthermore, high power lasers usually are employed, with which the conversion of incident radiation into CARS can be quite efficient. The disadvantages of these techniques is the limited optical access existing in the pre-burner, which restricts temperature profiling to a chord joining the existing access ports in the pre-burner. CARS also requires a knowledge of linewidths including the effect of temperature, and collision partner on the width.

The performance of a CARS measurement system for this application is enumerated in the following section for comparison to the other techniques.

The advantages of the Raman, fluorescence and CARS are summarized in Table II. The Raman techique looks to be the most favorable approach for SSME pre-burner diagnostics. The last row of this chart presents a comparison which has not been made so far. This is, the ease of implementation. The use of optical diagnostics in the vicinity of a rocket engine presents several challenges already described. One advantage of Raman scattering is that it appears quite feasible to use an optical fiber to connect to an optical head located on one side of the pre-burner. This would overcome many of the difficulties associated with operation of the engine, such as the motion associated with thrust load and gimballing, frosting and vapor condensation that occurs around the engine due to the cryogenic propellants and vibration and acoustic radiation.

Spontaneous Raman scattering appears to be the clear choice for SSME pre-burner optical diagnostics if signal magnitudes are adequate, and these are considered in the following sections.

Comparison of Optical Diagnostic Techniques

This section compares numerically the potential performance of the Raman scattering, CARS and laser fluorescence techniques for SSME pre-burner optical diagnostics. The diagnostic system performance is determined by pre-burner gas flow conditions and geometry. The pre-burner is assumed to be operating at the nominal power level at which the pressure is 38 MPa (5500 psi) and the temperature is 1000 K (1800 R). The gas composition is taken as indicated in Table I. The existing access ports are 1.1 cm (0.55 inches) in diameter and the combustor is about 25 cm (10 inches) in diameter. The available cw optical power in the pre-burner is fixed at 5 Watts, which is the approximate level allowable in an optical fiber of diameter appropriate for these measurements. The measurement spatial and temporal resolution are taken as 1 cm and 10 msec, respectively.

Raman Scattering

The Raman scattering signal power excited by an incident laser of power P_L is given by (Ref. 1)

$$P_R = P_L \left(\frac{d\sigma}{d\Omega}\right) n_J \Omega \epsilon_c \ell \qquad (1)$$

TABLE II

COMPARISON OF THE ADVANTAGES AND DISADVANTAGES OF APPLICABLE TECHNIQUES FOR SSME OPTICAL DIAGNOSTICS

Aspect	Raman	CARS	Fluorescence
Required geometry	Any geometry satisfying polarization requirements	Line-of-sight	Any geometry
Source requirement	Single laser	Two lasers	Single tunable laser or perhaps two lasers
Collection	Scattered into 4π steradian	Efficient collection possible	Scattered into 4π steradian
Analysis of data	No theoretical hurdles	Linewidth data required	Quenching rates required
Signal level	Adequate	Limited by approach	Low OH concentrations Other molecules inaccessible Possible seed required
Implementation	Optical fiber approach appears feasible	Optical fiber not feasible	Poor transmission of required UV light if not seeded

where n_J is the population of the J-th rotational level, $d\sigma/d\Omega$ is the differential Raman cross section, Ω is the collection solid angle, ϵ_c is the collection efficiency and ℓ is the sampling extent or spatial resolution. The Raman cross section for H_2 is $1.4 \times 10^{-30} cm^2$ steradian for a incident laser wavelength at 4880 Angstroms (Ref. 12). The solid angle for a 1 cm aperture at 13 cm, half the combustor diameter, is 0.004 steradians. Taking the collection efficiency as 10 percent and the sampling extent as 1 cm, the calculated Raman signal is 5.5×10^4 photons. This level of performance is shown in the next section to be adequate to meet program design goals. That section further considers the performance for practical system elements.

Coherent Anti-Stokes Raman Spectroscopy

CARS is a wave mixing technique requiring two frequencies. One laser supplies one frequency, called the pump, while another laser is used to supply the second frequency which is Stokes shifted with respect to the first. Two approaches are used to generate the CARS spectrum. In the first, the Stokes laser is scanned across the appropriate frequency interval, and the entire spectrum is generated successively. This approach is limited by the time needed to scan the laser. The second approach uses a wide bandwidth Stokes dye laser to generate the entire molecular spectrum at once.

The two approaches divide into continuous-wave and pulsed modes of operation because of the characteristics of dye lasers. Pulsed lasers afford gain over a broader spectral profile, and can have a bandwidth as broad as a few hundred wavenumbers, whereas cw dye lasers have bandwidths of 1 cm^{-1} or smaller. Both approaches have been considered for SSME pre-burner optical diagnostics.

The cw dye laser approach would use two or more dye lasers tuned to resonance with hydrogen molecular transitions. The CARS signal can be estimated from the expression for CARS power P_3 in terms of the laser powers (Ref. 1).

$$P_3 = \left(\frac{\omega_1}{\pi c}\right)^2 \left(\frac{4\pi^2 \omega_3}{c^2}\right)^2 \quad P_1^2 \; P_2 \quad |\chi|^2 \qquad (2)$$

where ω_1 is the pump frequency ω_3 is the anti-Stokes frequency, P_1 and P_2 are the pump and Stokes laser powers respectively. χ is the third order nonlinear susceptibility. Assuming the same pump power as in the other cases, and a dye

laser power of 0.2 W, which is typical of available cw dye lasers and a collection efficiency of 10 percent, the calculated CARS signal is 2×10^4 photons. It should be noted that this approach is costly due the expense of using two dye lasers. A typical commercial dye laser would have a bandwidth of 1 cm^{-1} and would require frequency stabilization to remain on the peak of the Raman shifted resonance, which is on the order of 0.4 cm^{-1}.

The second approach to CARS diagnostics uses a pulsed laser to provide the pump frequency and to pump a broadband dye laser. The usual output of a pulsed laser is too high to insert into an optical fiber, and would require considerable attenuation. Therefore the power is limited to 5 Watts for both the pump and Stokes lasers. A good choice for this laser may be a high repetition frequency Nd:YAG laser that has cw flashlamps and a Q-switched cavity. A typical laser of this type would have a pulse repetition frequency (prf) of 10 kHz and a pulse duration of 233 nanoseconds. In 10 milliseconds 100 pulses would be obtained giving a dye laser energy of 0.1 mJ. The estimated CARS signal count would be 2×10^3 photons for a 100 cm^{-1} wide dye laser.

The estimated signal magnitude depends critically on the laser power for nonlinear processes such as CARS. An optical fiber is expected to be capable of handling a higher intensity of pulsed radiation if the pulses are short enough in duration. The pulse duration must be shorter than the time required to traverse the optical fiber. For a 40 meter long fiber this time would be about 200 nanoseconds. Therefore, it is expected that slightly higher peak powers could be used in the case just described, but this gain would not be sufficient to offset the low signal. Nd:YAG lasers are commercially available which operate with much shorter pulses (10 nanoseconds), using pulsed flashlamps; however the prf is restricted to 10-20 Hz. This low frequency is incompatible with the desired temporal resolution.

Although the CARS approach would be more attractive with lasers intermediate between those two operating ranges, the CARS technique also has other disadvantages, aside from the requirement for through optical access. The nonlinear susceptibility depends on the Raman linewidth, which in the extreme conditions of the SSME pre-burner requires extrapolation of existing linewidth data. This would need to be verified in experiments. Another potential problem is frequency shifting, which for the cw approach may require retuning the Stokes laser to stay in resonance with the molecular transition. This can be accomplished through a variety of frequency stabilization approaches, but makes the instrument more complicated.

Laser Induced Fluorescence

The laser fluorescence power is a function of the laser intensity, the quenching rates of levels involved in the transition, the spontaneous emission rates and the frequency overlap with the absorbing molecular frequency (Refs. 3 and 4). The fluorescence power varies linearly with laser power at low power, but reaches a constant value at high powers when the radiation is intense enough to saturate the molecular transitions.

The expression for the fluorescence power, S_F, assumes a simple form at saturation

$$S_F = h\nu_F \, A_{21} \, \Omega \, V_C \, N_{1J} \qquad (3)$$

where h is Planck's constant, ν_F is the transition frequency, A_{21} is the radiative transition rate, Ω and V_C are the solid angle and volume respectively from which fluorescence is collected and N_{1J} is the population of the lower (absorbing) state involved in the transition. For the pre-burner conditions the most populated lower level, J' = 4.5, in the notation adopted for spin-orbit coupling, has a population of $1.0 \times 10^7 cm^{-3}$. The radiative lifetime is 0.803 microsecond (Ref. 13). It is estimated that in 10 milliseconds, 1.1×10^4 photons would be collected which compares closely with the signal for the equivalent H_2 spontaneous Raman system.

It is not likely that the transition involved in the transition can be saturated because of practical limitations on the incident laser power. Lucht, Sweeney and Laurendeau (Ref. 14) using a dye laser pumped by a Nd:YAG laser observed fluorescence from the directly excited J' = 4.5, N' = 4 upper rotational level using a spectrometer tuned to the $P_1(5)$ transition. At atmospheric pressure the power needed to saturate the transition was 150 kW (at ~ 3100A). This value can be scaled linearly to the pressure conditions of the SSME pre-burner. Therefore at the nominal conditions obtained in the pre-burner the saturation intensity would be about 55 GW corresponding to intensities in excess of 7 TW/cm^2 in optical fibers of 1 mm diameter or less. This intensity is far in excess of the levels considered for this application. It means that the photon count estimated from Eq. (3) is too high, the actual count attainable would be lower.

Technique Selection

Within the constraints imposed on optical access to the SSME pre-burner the selection of the optimum technique is clear. CARS and other coherent techniques afford only temperature measurement along a line in the pre-burner defined by the chord joining the two existing transducer ports. CARS and like techniques can yield large signal with unlimited laser power, but when the power is limited to levels amenable to transmission through an optical fiber, the signal level is no higher than spontaneous Raman scattering. Another potential problem of a lesser nature is associated with the Raman linewidth at these gas conditions. Analysis of CARS spectra would require a knowledge of the widths of individual transitions. Existing data do not apply to the pre-burner conditions; therefore additional measurements of these would be required.

Laser induced fluorescence signal levels are predicted to be far below the other techniques for equivalent diagnostic conditions, due to the low concentrations of fluorescing species, namely OH. The probing of molecular levels in OH would require a source emitting in the ultraviolet and more importantly, the transmission of uv radiation through an optical fiber. The absorption of fibers generally rises in the short wavelength region of the optical spectrum due to Rayleigh scattering, making the transmission of uv relatively poor. Since saturation of the fluorescent transition is not practical, a knowledge of quenching rates is also required. The use of a seed material could increase fluorescence levels, but may be difficult to implement. This is an unnecessary complication since the Raman technique appears capable of achieving the diagnostic design goals without seeding.

The spontaneous Raman backscattering approach alleviates all of the aforementioned objections. It appears practical to make temperature measurements using this technique. This has been indicated somewhat by the calculations shown thus far, but calculations shown in the next Section of this report carry the predictions further. One drawback, to be considered with Raman scattering is the relatively low collection efficiency imposed by the limited window size in the SSME pre-burner. The very high density offsets this limitation however. Frequently in practical combustion measurements the background radiation due to flame emission limits the Raman signal-to-noise ratio. However the hydrogen flame exhibits extremely low visible emission in the laboratory. This is also expected to be the case in the pre-burner due to the fuel-rich condition. Detailed knowledge of the linewidth and line shift of transitions is not needed for Raman temperature measurements. One only needs to be satisfied that the transitions do not become so broad that there is appreciable overlap. This is not expected, as will be shown in the next section. The theory of Raman scattering in hydrogen is among the most well known, so that no theoretical hurdles are expected for the analysis of data. Finally and very significantly the Raman backscattering approach appears to be amenable to implementation with optical fibers. Furthermore only one laser source is required, ameliorating the expense and practical problems associated with operating two lasers.

SPONTANEOUS RAMAN DIAGNOSTIC SYSTEM

This section describes spontaneous Raman scattering diagnostics, selected as the best technique for SSME pre-burner optical diagnostics. This section begins by describing the principles of Raman temperature measurements as applied to the fuel pre-burner. The theory of hydrogen Raman line intensities, and lineshapes is presented. The implications for diagnostics of the two possible nuclear spin orientations in hydrogen are identified and the results of calculations for the nominal power condition are presented. Following this the design of the optical diagnostic system is considered. The use of optical fibers is examined and the desired characteristics of other system elements such as the spectrometer, detector and laser are enumerated. Finally the performance of the Raman diagnostic system is estimated, and evaluated in terms of program design goals.

Principles of Raman Diagnostics

Theory of Hydrogen Raman Intensities

The calculation of theoretical Raman spectra is straightforward. Raman spectroscopy is well presented in recent reviews (Refs. 5-7). In the usual prescription, the Raman scattered power P_R is related to the incident laser power by

$$P_R = P_L \left(\frac{d\sigma}{d\Omega}\right) n_J \Omega \ell \qquad (4)$$

where $d\sigma/d\Omega$ is the Raman cross section, n_{vJ} is the population density, ℓ is scattering length, and Ω is the solid angle over which Raman scattered radiation is collected. This simple expression is inadequate for the expression of Raman scattering powers in hydrogen, because of the effects of the rotational-vibrational interaction. This factor which is most important for anharmonic oscillators, results from the perturbation of the vibrational energy levels by centrifugal distortion of the molecule in higher rotational levels. James and Klemperer (Ref. 15) first studied this factor, which is analogous to the Herman-Wallis correction to the transition dipole moments in infrared spectroscopy. The correction factors for H_2 and other atmospheric gases are described by Asawaroengchai and Rosenblatt (Ref. 16). These factors have been used in the calculations presented here. Recently Cheung et al. (Ref. 17) calculated more accurate centrifugal distortion factors. These result in a difference of less than 2% for the tenth rotational level, therefore analytic expressions of James and Klemperer have been retained.

Raman scattering arises from the induced polarizability of the molecule, that is the relative response of the electron cloud and the nuclei to the electromagnetic field of the incident radiation. The polarizability is a tensor which can be decomposed into an isotropic part and an anisotropic part. For diatomic molecules the anisotropic part is simply $\beta = \alpha_{\parallel} - \alpha_{\perp}$, where $\alpha_{\perp}$ is the polarizability element perpendicular to the nuclear axis and $\alpha_{\parallel}$ is the component parallel to the axis. The isotropic part is $\alpha = (\alpha_{\parallel} + 2\alpha_{\perp})/3$.

The intensity of a Raman molecular transition in terms of energy flux scattered from unit volume per solid angle is given by:

$$I_R = \left(\frac{2\pi \nu_S}{c}\right)^4 \frac{N_{vJ}}{2J+1} \langle \alpha \rangle^2 I_L \qquad (5)$$

where I_o is the energy flux of the incident radiation, ν is the frequency of the scattered radiation, N_{vJ} is the density of scattering molecules, v and J are the vibrational and rotational quantum numbers respectively and $\langle \alpha \rangle^2$ is the square of the polarizability matrix element. The matrix element squared can be written in the form (Ref. 15)

$$\langle \alpha \rangle^2 = C_b \, S(J) \, f(J) \qquad (6)$$

where C_b is an intensity factor which depends on the rigid rotator polarizability, S(J) is the rotational line strength and f(J) is a correction for the centrifugal distortion caused by vibrational-rotational interaction, derived by James and Klemperer (Ref. 15).

The line strength for J -> J + 2 pure rotational Stokes (O-branch) scattering and Stokes vibrational-rotational S-branches is

$$S(J, J+2) = \frac{(J+1)(J+2)}{2J+3} \qquad (7)$$

and the line strength for J -> J - 2 transitions is (S-branch)

$$S(J, J-2) = \frac{(J-1)\,J}{2J-1} \tag{8}$$

James and Klemperer showed that for pure rotational Stokes transitions

$$f(J)^{S}_{00} = \left[1 + \left(\frac{4}{\chi}\right)\left(\frac{B_e}{\omega_e}\right)^2 (J^2 + 3J + 3)\right]^2 \tag{9}$$

where $\chi = \beta_e / r_e \beta_e'$, β_e' is the first derivative of the polarizability anisotropy, r_e is the equilibrium nuclear separation and B_e and ω_e are the rotational and vibrational constants respectively. For anti-Stokes transitions

$$f(J)^{O}_{00} = \left[1 + \left(\frac{4}{\chi}\right)\left(\frac{B_e}{\omega_e}\right)^2 (J^2 - J + 1)\right]^2 \tag{10}$$

where here the notation has been changed somewhat in that J denotes the rotational quantum number of the initial state, so that the transition considered is J -> J - 2.

For rotational-vibrational transitions the f correction factors are given by:

S-branch
$$f(J)^{S}_{01} = \left[1 - 3\left(\frac{B_e}{\omega_e}\right)^2 J(J+1) - 4\chi\left(\frac{B_e}{\omega_e}\right)(2J+3)\right]^2 \tag{11}$$

O-branch
$$f(J)^{O}_{01} = \left[1 - 3\left(\frac{B_e}{\omega_e}\right)^2 J(J+1) + 4\chi\left(\frac{B_e}{\omega_e}\right)(2J-1)\right]^2 \tag{12}$$

Q-branch
$$f(J)^{O}_{01} = \left[1 - 3\left(\frac{B_e}{\omega_e}\right)^2 J(J+1)\right]^2 \tag{13}$$

The rigid rotor intensity factor C_b is given in terms of the molecular polarizability components which are summarized in Table III. β_0 is the polarizability anisotropy for $v = 0$, r_e is the equilibrium internuclear radius and β_e' is the first derivative of the polarizability anisotropy $(d\beta/dr)r_e$.

TABLE III

MOLECULAR POLARIZABILITY FACTOR, C_b $(v = 0)$

Pure rotation: $C_b = (7/30)\ \beta_0^2$

Vibration-rotation $C_b = (7/30)\ (r_e\beta_e')^2\ (B_e/\omega_e)$

The corresponding relationship for the Q-branch intensity is not expressible as a simple factor. James and Klemperer explicitly derived the expression for the case of Raman scattering being observed at 90 degrees to the direction of propagation of the exciting radiation, but the expression for backscatter can be written down from their equations. The corresponding expression for the Q-branch intensity in the backscatter direction is

$$I_{01}^{Q} = (2\pi k_s)^4 \left(\frac{B_e}{\omega_e}\right) f_{01}^{Q}(J)\, N_{OJ} \left[(r_e\, \alpha_e')^2 + \mathcal{S}(J)(r_e\,\gamma')^2/(2J+1)\right] \quad (14)$$

where

$$\mathcal{S}(J) = \frac{1}{15}\frac{J(J+1)(2J+1)}{(2J+3)(2J-1)} - \frac{2J+1}{9} + \frac{4}{15}\frac{J(J+1)}{2J+1} + \frac{\mathcal{N}(J)+\mathcal{N}(J-1)}{15} \quad (15)$$

and

$$\mathcal{N}(J) = \frac{J(4J^2+1)}{(2J+1)(2J-1)} \quad (16)$$

The parameters used to evaluate these expressions are summarized in Table IV. The centrifugal distortion factors have been evaluated for the rotational energy levels populated in the SSME pre-burner flow conditions. Rotational levels up to J = 5 or 6 are significantly populated. The centrifugal distortion factor is 1.243 for an S-branch transition from this level and 1.129 for an Q-branch transition. These contributions will be important for accurate diagnostic measurements. Rosenblatt and co-workers (Ref. 17) made more accurate ab initio calculations of these factors and found differences with Eqs. (9-13) that are important for rotational levels J > 8, and are therefore significant only in hotter flames T > 1800.

TABLE IV

POLARIZABILITY MATRIX ELEMENT DATA

Quantity	Value	Reference
β_0	0.314×10^{-24} cm^3	16
χ	0.38	16
α'	1.230×10^{-16} cm^2	18
γ'	1.02×10^{-16} cm^2	16
r_e	0.741×10^{-8} cm^2	16

Hydrogen Lineshapes

The linewidths and frequencies of Raman lines are affected by atomic and molecular collisions. An increase in pressure can cause broadening and shifting of the Raman lines of hydrogen. Considering the extreme pressures existing in the SSME pre-burner it is important to determine the magnitude and impact of these effects on optical diagnostics.

Pressure broadening and shifting has been the subject of numerous investigations because intermolecular forces can be studied by measuring the effects of pressure and temperature on spectral linewidths (Ref. 19). At low pressures (less than 0.1 atmospheres) and moderate temperatures, the Raman linewidth is Doppler broadened and its shape is Gaussian. At pressures greater than 10 atmospheres the Raman linewidth is pressure broadened, the linewidth increases linearly with gas density, and the lineshape is Lorentzian. The linewidth is proportional to $B\rho$, where B is the optical (Raman) broadening coefficient and ρ is the density, normally in amagats. In the range of densities between the Doppler limit and the pressure broadening regime, line narrowing, named for Dicke who first described it (Ref. 20) occurs in hydrogen. Doppler broadening for a scattering event arises from the recoil momentum imparted to the molecule by the scattering photon. If an elastic collision occurs simultaneously with the scattering event, some of the momentum may be taken up by the colliding molecule; and the scattered photon will have a smaller Doppler shift than if no collision had occurred. Pressure broadening becomes dominant when the collision rate is so large that a substantial number of inelastic collisions occur, which change the internal state of the molecule. Dicke narrowing takes place when the mean free path for elastic collisions is comparable to the wavelength of the scattered photon and is less than the mean free path for line broadening (Ref. 21).

As the density is increased another narrowing mechanism is manifested in the Raman lines of most molecules. Collision or motional narrowing occurs when closely spaced Raman lines broaden into one another, and the transitions can no longer be considered to be individual transitions. This occurs at quite low pressures in common atmospheric gases. Due to the very large frequency spacing of lines in hydrogen it does not occur until densities corresponding to several thousands of atmospheres have been reached (Ref. 22).

The Raman linewidths corresponding to rotational and vibrational transitions have somewhat different broadening coefficients due to differences in the effective collision mechanisms which affect the two types of transitions. This has been discussed by Srivistava and Zaidi (Ref. 19). The reason for the difference is that rotational linewidths are the result of elastic and inelastic collisions. Therefore the rotational linewidth is broader than the vibrational linewidth. Table V shows the broadening coefficients at 300 K. There is very little data on the effect of temperature on the Raman broadening coefficients. Lallemand and Simova (Ref. 23) measured the broadening coefficient from 300 to 425 K. Their data indicate a $T^{1.25}$ temperature dependence for the Q-branch transition Q(1). Assuming the broadening coefficient varies with this temperature dependence and taking an average broadening coefficient at 300 K of .0025 cm^{-1}/amagat the estimated linewidth at SSME pre-burner conditions (5500 psia, 1000 K) is approximately 0.5 cm^{-1}. This is less than the expected spectral resolution of the spectrograph to be used and therefore the actual linewidth is not critical.

TABLE V

RAMAN BROADENING COEFFICIENTS

Rotational Transition	Linewidth x 10^{-3} (Ref. 24)	(Ref. 25)	(Ref. 26)
$S_0(0)$	2.80	3.1	3.0
$S_0(1)$	3.47	3.8	4.6
$S_0(2)$	?.47		
$S_0(3)$	2.53		
$S_0(4)$	1.53		

Vibrational Transition	Linewidth x 10^{-3} (Ref. 27)	(Ref. 28)	(Ref. 26)
$Q_{01}(0)$	2.32		
$Q_{01}(1)$	1.40	1.68	1.90
$Q_{01}(2)$	2.53		
$Q_{01}(3)$	3.66		

Similarly the effect of pressure on the frequency of Raman transitions has been measured in hydrogen (Ref. 19). The shift is approximately -0.2 cm^{-1}/100 amagats at 300 K (Ref. 23) for the Q(1) transition. Lallemand and Simova (Ref. 23) found the linear pressure shift coefficient to vary linearly with temperature from 80 to 500 K, becoming positive for temperatures above 420 K. Extrapolating these data to the operating conditions of the SSME pre-burner, the shift is very roughly estimated to be on the order of +1 cm^{-1}. Rotational shifts have been found to be smaller (Ref. 26). There is little impact on optical diagnostics expected due to these shifts.

The Effects of Ortho and Para Hydrogen Modifications

Hydrogen has a nuclear spin of 1/2. Different orientations of the two nuclear spins with respect to one another give rise to two molecular modifications designated as ortho and para. In the ortho form, the nuclear spins are aligned parallel, and in the para form the spins are anti-parallel. The states with even rotational quantum number J belong to the para-modification, while the odd-J states belong to the ortho-modification. The relative equilibrium composition depends on the temperature. At room temperature hydrogen is 75 percent ortho-hydrogen, but at the normal boiling point, 20.4 K, hydrogen is 99.79 percent para-hydrogen.

The conversion of ortho to para is slow in the absence of catalysts at low to moderate temperatures so that it is quite possible to have a composition that differs greatly from equilibrium. The conversion of hydrogen from the ortho-form to the para-form is accompanied by the release of 1.06 kJ/mole of heat at the normal boiling point (Ref. 29). The heat generated in this reaction is comparable to the heat of vaporisation, so that this reaction can account for boil-off losses in liquid normal-hydrogen (75 percent ortho-hydrogen) of about 1% per hour (Ref. 29), which are unacceptable in most applications. The boil-off losses in the pure para-modification, however due to the absence of conversion, can be minimized by good tank design practices to levels below 1 percent per day. Therefore hydrogen is almost always converted catalytically to the para-modification during liquefaction.

The direct spontaneous transition from ortho to para through spin-interchange is strictly prohibited (Ref. 30). Self-conversion takes place through atom-exchange:

$$H + p\text{-}H_2 \rightarrow o\text{-}H_2 + H \qquad (17)$$

This reaction does not violate the prohibition of spin interchange because a new molecule is formed in the reaction. The atoms are supplied in this reaction by dissociation of molecular hydrogen. Spontaneous conversion was studied by Farkas and Farkas (Ref. 31). Subsequent measurements suggested that the earlier results were affected by small quantities of oxygen in the hydrogen stream (Ref. 32). The reaction time t, is related to the reaction rate constant k (Refs. 33, 34), and the equilibrium constant K, by the relation

$$t^{-1} = k K \left[H_2\right] \qquad (18)$$

The time calculated from this relation at the conditions existing in the SSME pre-burner is approximately 2 sec. This assumes that the mechanism which has been confirmed at low pressures does not change over several orders of magnitude in the pressure. Oxygen present in the SSME pre-burner will affect the H-atom concentration and also catalyse the converion of para-hydrogen into ortho-hydrogen (Ref. 32), so that actual conversion rates will be faster than the self conversion rate calculated here.

The characteristic reaction time for self conversion is longer than the residence time in the pre-burner. Therefore it is possible that the hydrogen ortho-para composition is not in equilibrium. This will affect the predictions of the rotational state populations in the measurement volume. Since the para modification dominates at low temperature it means that the even rotational levels will be more highly populated than predicted from equilibrium, tending to minimize the differences in the two manifolds. The impact of these considerations is on the analysis of the data. When the relative populations are analyzed, the even and odd rotational levels must be considered separately. Both rotational manifolds should yield a valid temperature, and this can serve as a check on the consistency. The total populations will not be greatly affected so that the predictions of Raman scattering signals still remain a valid estimate of the system performance.

Results of Raman Calculations

Calculations have been performed based on the theoretical development described for the effects of anharmonicity on the hydrogen Raman intensities. The calculations are illustrated in Figs. 2 and 3. The first of the figures depicts the calculated Raman spectrum of hydrogen at 38 MPa (5500 psi) and 1000 K corresponding to the nominal conditions in the fuel pre-burner. The Raman intensities are shown as a function of Raman shift from the exciting wavelength, 4880 A for the calculation shown. The pure rotational Raman transitions corresponding to the O ($\Delta J = -2$) and S ($\Delta J = +2$) branches are shown with negative and positive frequency shifts respectively. The vibrational Q-branch ($\Delta v = 1$, $\Delta J = 0$) is shown near 4160 cm^{-1} shift, with associated vibrational O and S branches near it. The various transitions arise from individual rotation transitions. The rotational S branch is nearly 2 times stronger than the vibrational Q branch at these conditions, indicating that rotational Raman would produce better system performance.

The sensitivity of the distribution of these rotational lines to gas temperature is shown in Fig. 3. The rotational quantum number of the initial level of the transition is shown in the bottom spectrum in the figure. The sensitivity of the distribution of the lines is shown. How temperature is deduced from Raman intensities is described in the next section.

Appendix A contains the output from a computer program based on the formulation described earlier. This tabulation gives for the various transitions the Raman shift, the wavelength of the shifted line, the molecular populations and the Raman intensities.

FIG. 2

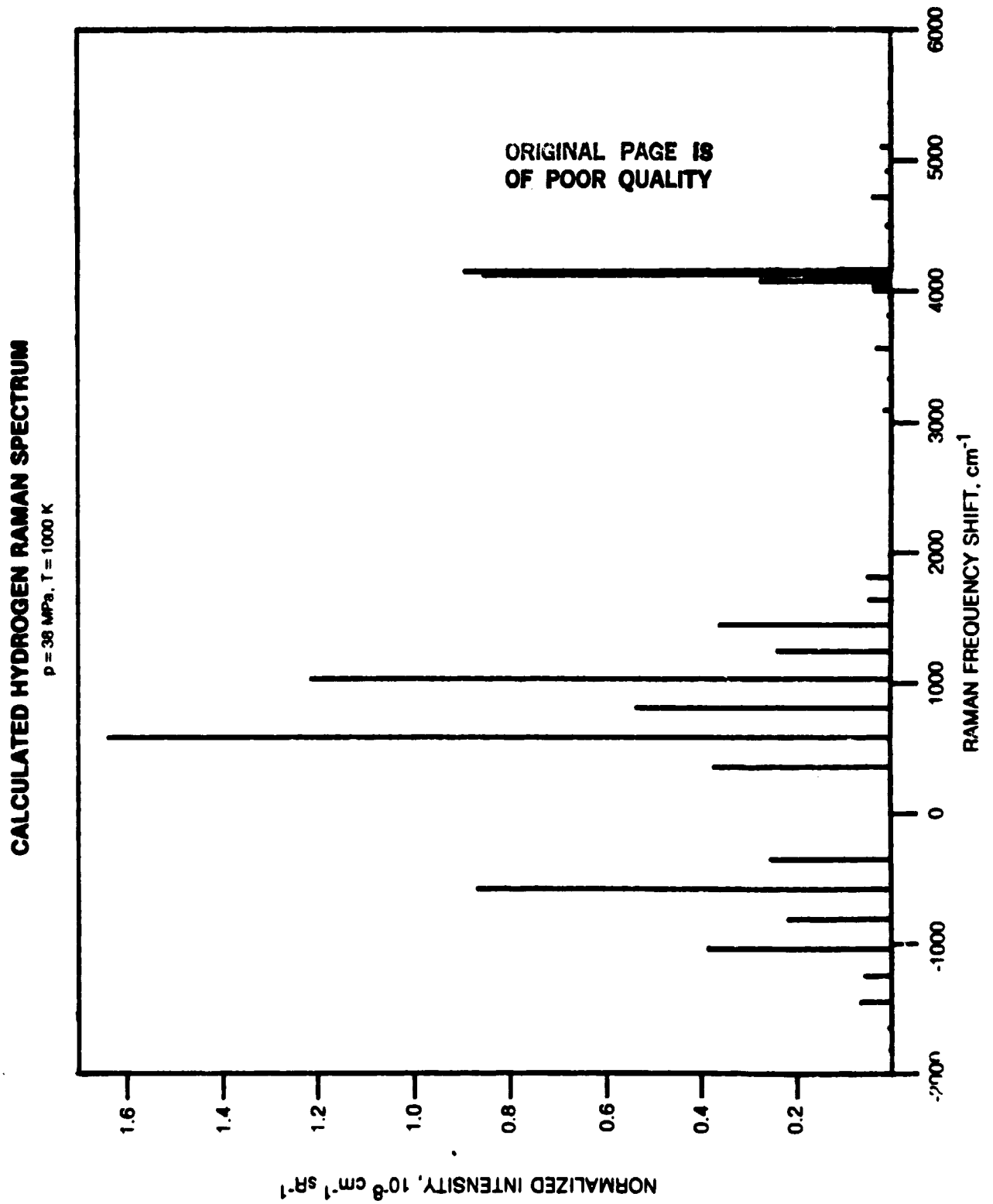

83-8-129-2

FIG. 3

TEMPERATURE DEPENDENCE OF CALCULATED RAMAN SPECTRA

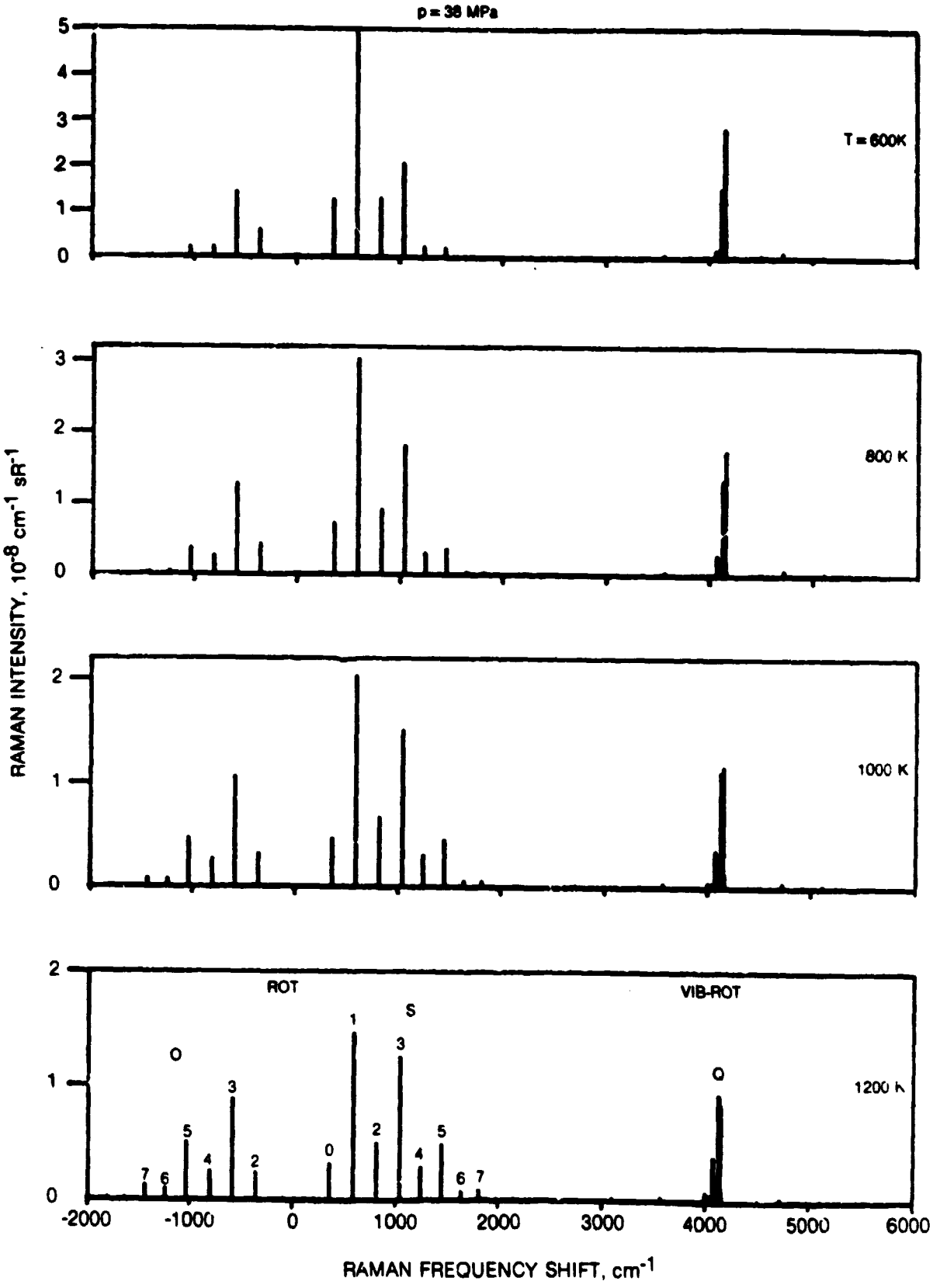

83-5-129-10

Raman Temperature Measurements

The sensitivity of the hydrogen Raman intensities to temperature is shown in Fig. 4. In practice, the gas temperature is determined from measured Raman intensities by appropriately normalizing and plotting them on a semi-logarithmic plot as a function of the rotational energy of the lower level involved in the transition. The principle of this procedure is illustrated in Fig. 4, which shows the normalized Raman intensity distribution for four temperatures from 600 to 1200 K. Normally the Raman signal would be in units of photon or photoelectron counts from a detector. These signal intensities are normalized by dividing by $\nu^3 g(J)S(J)f(J)/R(\nu)$ where $R(\nu)$ accounts for the spectral response of the optical system, a factor which must be determined empirically with a standard spectral lamp. The temperature is determined from the slope of these lines, m, since $m = hc/kT$. As a practical matter the line intensities may need to be determined by integrating across the spectral width of the lines on the multichannel optical detector.

System Design Considerations

The system for the SSME pre-burner optical diagnostics is conceived as composed of a high power laser, an optical head mounted directly on the preburner, and a spectrograph/optical multichannel detector (OMD) combination. The laser and the spectrograph/OMD would be located remotely, and would be joined to the optical head by optical fiber links. The use of optical fibers is crucial to this application because of the severe environment surrounding the operating engine. The theoretical limits to propagation of high power laser radiation are discussed in the next section. Following that is a discussion of the selection of the laser source. Lastly the requirements for the spectrograph/detector combination are evaluated. The elements of the diagnostic system are shown in Fig. 5.

Power Handling Capability of Optical Fibers

The power handling capability of low-loss optical fibers is generally limited by nonlinear processes occuring in the fiber for visible and near infrared radiation. The surface quality and finish of the fiber end also can affect the critical power for fibers carrying ultraviolet radiation.

The theoretical power handling capacity of small diameter (single mode) low-loss optical fibers was investigated by Smith (Ref. 35). He found that stimulated Raman and stimulated Brillouin inelastic scattering determine the practical power capacity of fibers at high power densities. In Raman scattering, the pump laser radiation field interacts inelastically with the nuclear vibrational mode

FIG. 4

TEMPERATURE DETERMINATION FROM NORMALIZED RAMAN INTENSITY

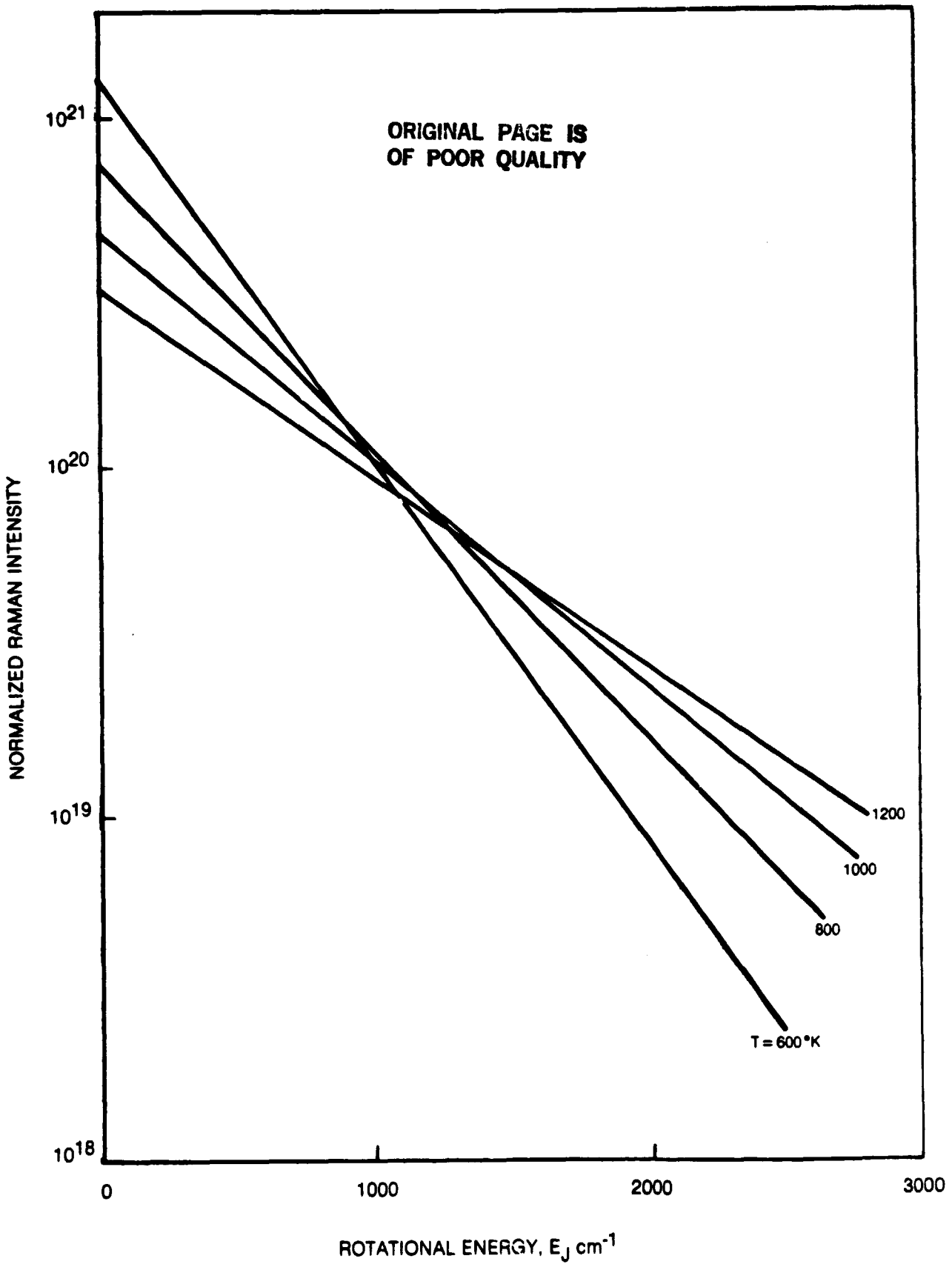

83-6-68-1

FIG. 5

ORIGINAL PAGE IS
OF POOR QUALITY

RAMAN DIAGNOSTICS SYSTEM

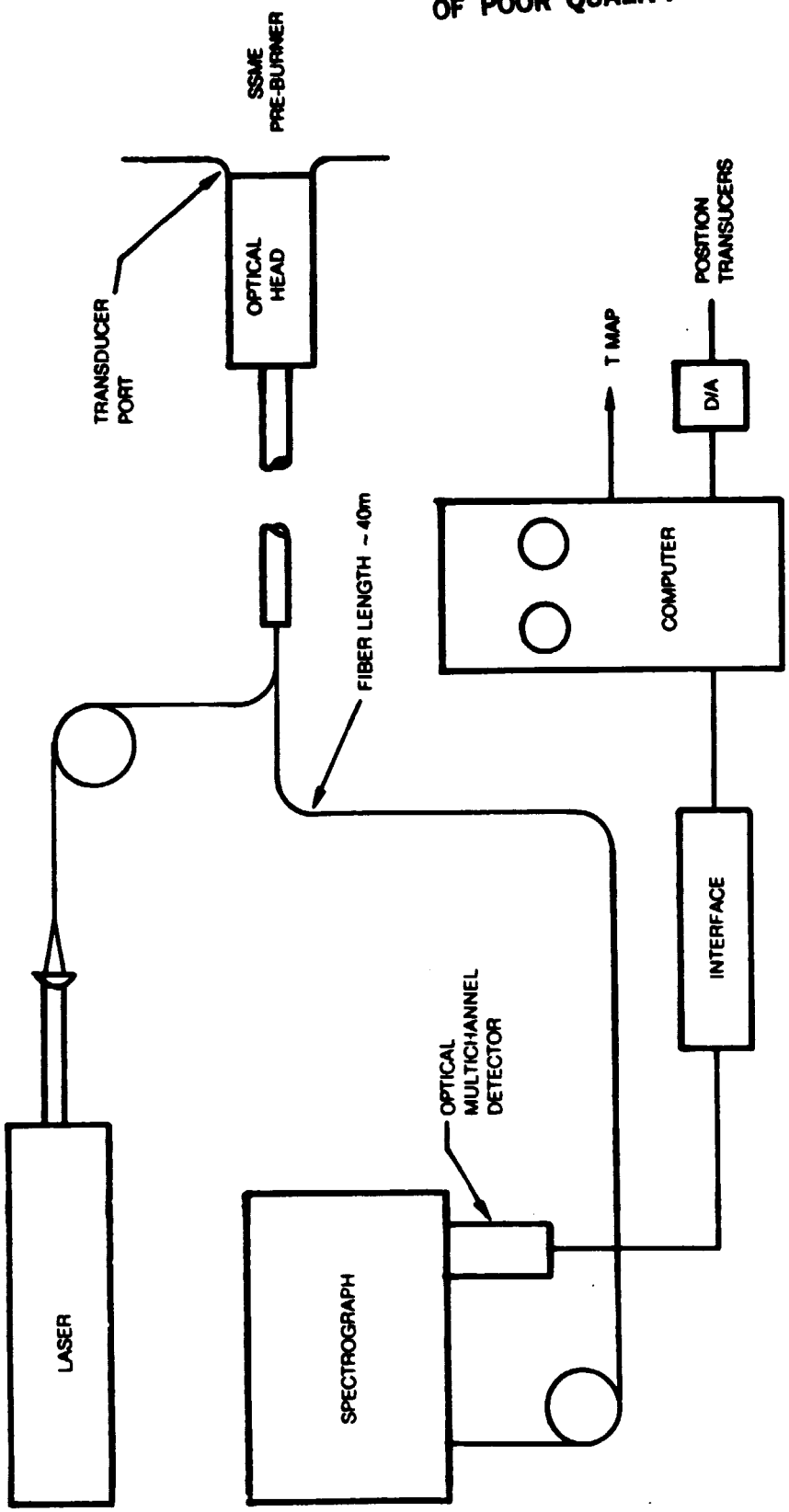

83-6-68-2

to produce a frequency which is down-shifted by the nuclear vibrational frequency. In stimulated Raman scattering, the optical wave itself produces a coherent wave in the nuclear vibrational coordinate which interacts with the transmitted optical beam. Stimulated Brillouin arises from the coherent acoustic wave driven by the optical field. The difference between Raman scattering and Brillouin scattering is that the former excites an optical phonon while the latter excites an acoustic phonon. For forward scattered Raman, the principal effect is to cause the pump frequency to be shifted and broadened. Backward processes, either Raman or Brillouin, can result in severe attenuation of the forward traveling optical wave, due to the stimulated backward wave, and therefore pose a more severe limitation to fiber power transmission.

The criterion that Smith chose to determine the critical power for nonlinear processes was taken arbitrarily to be that power for which the optical field generated by the nonlinear interaction is comparable to the incident field. These optical processes depend exponentially on the pump power level, so that a reduction of the pump power level of 1 dB, reduces the stimulated scattering level by 20 dB (Ref. 35). Therefore the calculated critical power level serves as a useful benchmark.

Smith assumed that the pump laser radiation propagates in the fiber as

$$P_p(Z) = P_p(0) \exp(-\alpha_p Z) \qquad (19)$$

where Pp(z) is the pump power at position z along the fiber, Pp(0) is the incident power and α_p is the attenuation coefficient at the pump wavelength. This means in effect that the pump field is not affected by the nonlinear interaction. Based on the above definition of critical power, Smith derived the following expression assuming the fiber length is much greater than the absorption length

$$\frac{\sqrt{\pi}}{2} hc^2 k_s \left(\frac{\gamma_0}{A\alpha_p}\right) \Delta k f = \left(\frac{\gamma_0 P_c}{A\alpha_p}\right)^n \exp\left(-\frac{\gamma_0 P_c}{A\alpha_p}\right) \qquad (20)$$

where h is Planck's constant, ν is the Stokes shifted frequency (Raman or Brillouin), γ is the nonlinear gain coefficient, A is the fiber cross-sectional area, and Δk is the Raman or Brillouin linewidth (FWHM). The factor f and the

exponent n depend on the stimulated process. For forward Raman scattering $n = 3/2$ and for backward nonlinear processes $n = 5/2$. The factor f is 1 for Raman scattering (forward or backward) and for Brillouin scattering $f = kT/h\nu_a$ where ν_a is the frequency of the acoustic phonon.

In order to evaluate the critical power it is necessary to know the gain and attenuation coefficients for the optical fiber at the wavelength of interest. For wavelengths in the visible away from the hydroxyl absorption bands near 0.7-1.4 micron, the attenuation coefficient can be estimated from Rayleigh scattering (Ref. 36). The estimated absorption coefficient is

$$\alpha_p = 2.6 \times 10^{-6} \lambda_p^{-4} \tag{21}$$

where the wavelength λ_p is in microns and the absorption coefficient is in units of cm^{-1}. The absorption coefficient in this formula corresponds to an attenuation of 1.7 dB/km at 0.9 microns. Stolen (Ref. 37) has found that the Raman gain coefficient scales linearly with pump frequency while the Brillioun gain coefficient is almost independent of pump frequency. Taking the gain coefficients from Smith (Ref. 35) then the appropriate gain coefficients are

$$G_R = 5 \times 10^{-10} \lambda_p^{-4} \quad \text{cm/w} \tag{22}$$

$$G_B = 3 \times 10^{-9} \quad \text{cm/w} \tag{23}$$

where λ_p is the pump wavelength is microns (Ref. 37). Smith found that the solutions of Eqs. (20) are not sensitive to the Stokes frequency, the linewidth or the factor f. The solutions yield (Ref. 35)

$$P_C = \frac{16 A \alpha_p}{G_R} \text{ watts} \tag{24}$$

$$P_C = \frac{21\, A\, \alpha_p}{G_B} \quad \text{Watts} \tag{25}$$

The critical intensity then is given by

$$I_C^R = 8.32 \times 10^4\ \lambda_p^{-3} \quad W/cm^2 \tag{26}$$

$$I_C^B = 1.82 \times 10^4\ \lambda_p^{-4} \quad W/cm^2 \tag{27}$$

where again the wavelength is in microns. These formulae are derived assuming that the fiber is longer than the absorption length, i.e. $1/\alpha_p$. For radiation at 0.4 microns wavelength, this length must be in excess of 100 meters. This length is much longer than the length contemplated for SSME pre-burner optical diagnostics. In this case the formulae for the critical powers are modified by replacing $1/\alpha_p$ by the effective length, l_{eff}:

$$l_{eff} = \frac{1 - \exp(-\alpha_p\, l)}{\alpha_p} \tag{28}$$

and l is the actual length of the fiber. The critical powers for stimulated Raman and Brillouin scattering are shown together in Fig. 6. A strong dependence on wavelength is predicted. This is due to the sharp increase in absorption for shorter wavelengths which attenuates the stimulated wave increasing the power that the fiber can handle before these processes become severe. For wavelengths as short as 0.4 microns the transmission for the 40 m length considered is greater than 80 percent.

The analysis above is relevant when there is no reflection from one of the ends of the fiber. Labudde, Anliker and Weber (Ref. 38) pointed out that when both reflectivities are finite an optical resonator is formed with a threshold pump power P_t given by

$$R_1 R_2 \exp\left(\frac{g P_t L_{eff}}{A}\right) \exp(-\alpha L) = 1 \tag{29}$$

ESTIMATED CRITICAL POWER IN FUSED SILICA FOR STIMULATED PROCESSES

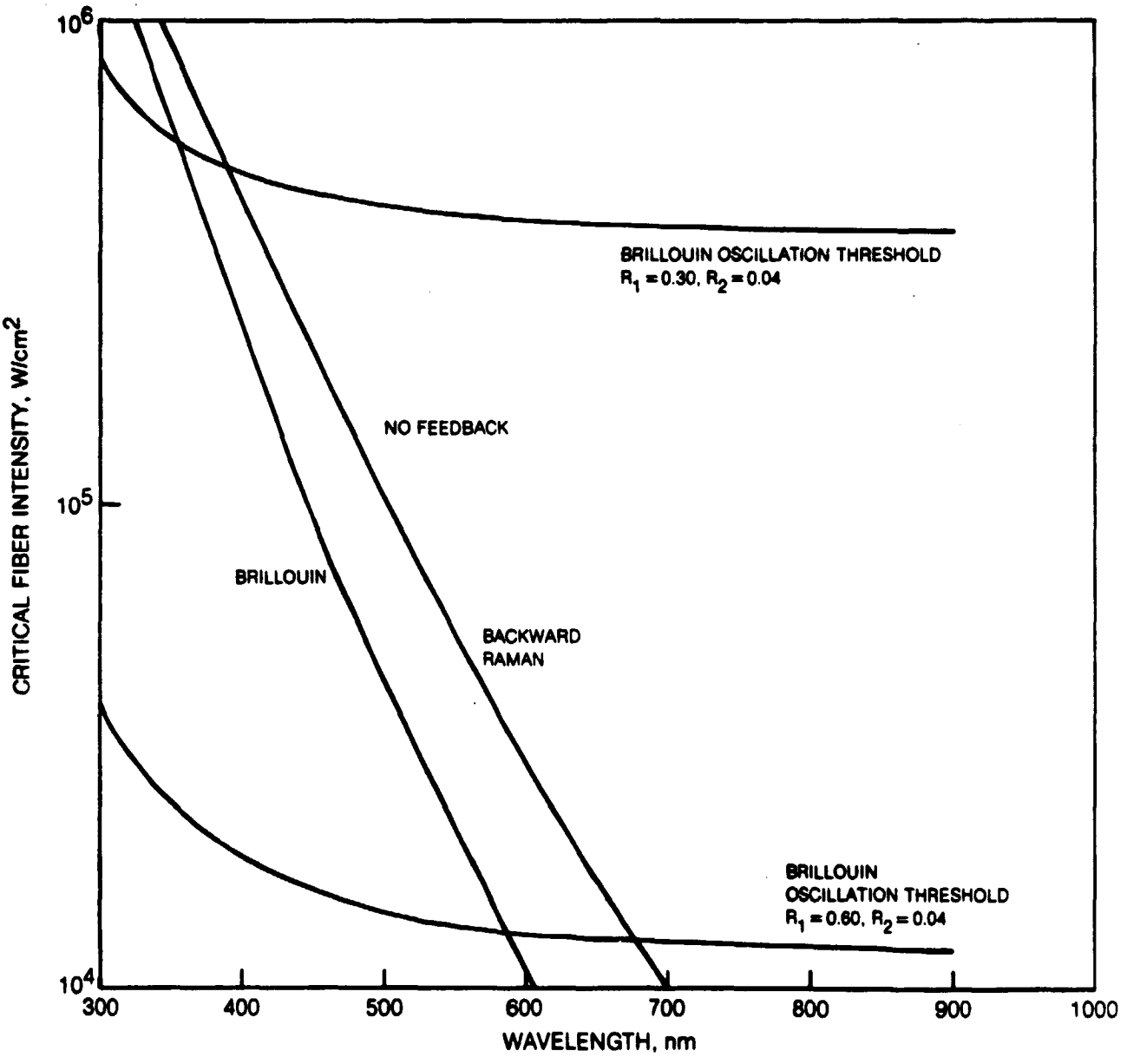

83-5-129-3

Labudde et al. also pointed out that when a laser is coupled directly into the end of the fiber the laser output mirror contributes to the effective reflectivity of the fiber. In experiments these authors used a Glan-Thompson prism and quarter wave plate combination to decouple the laser from the fiber, noting that this is only partially effective because the backscattered light, which is unpolarized due to polarization scrambling in the fiber, is attenuated by only 50 percent in the isolator. The critical threshold intensity for Raman and Brillouin scattering calculated from Eq. (29) is shown in Fig. 6 for two end reflectivity combinations, by curves labelled "Brillouin oscillation threshold". The lower curve corresponds to the case when there is no coupling isolation and shows its importance. The decrease in critical intensity with wavelength is not as severe as before because of the dependence on the effective length. The critical Raman intensity increases at longer wavelength because of the lower gain coefficient. Since the Brillouin gain is independent of wavelength, its critical intensity just decreases with wavelength. Comparing the curves shown in Fig. 6, it is seen that the critical intensity for wavelengths around 0.5 microns is limited by the feedback from the ends of the fiber by Brillouin scattering. When the effective fiber end reflectivity is larger than 0.30, the critical intensity is even lower.

These considerations apply to the transmission of a single transverse mode through the fiber. The power limitation for a single mode fiber is on the order of tens of milliwatts. This is too small for SSME pre-burner optical diagnostics, therefore the use of multimode fibers is envisioned. The critical power is correspondingly higher for multimode fibers (Ref. 35). Table VI shows the critical power per transverse mode calculated for an intensity limit of 40 kW/cm^2, which Fig. 6 indicates is reasonable for Brillouin scattering. The values shown are per transvese mode. Typically an argon ion laser such as envisioned for these measurements would excite several transverse modes, so that the use of total power 5-10 times these figures seems reasonable.

TABLE VI

CALCULATED CRITICAL POWER PER TRANSVERSE MODE

Diameter (micron)	P_{crit} (W)
50	0.784
100	3.14
150	7.08
200	12.6

Smith points out that the critical power for fibers can be higher for pulsed laser sources. The analysis above is applicable only to cw laser sources. When the pulse duration is less than the time required to traverse the fiber then the laser pulse does not interact with the generated stimulated radiation along the full length of the fiber. For the length of fiber envisaged for this application the pulse duration would need to be less than about 100 nanoseconds for this effect to be important. This does not lead to large increases in the critical power for pulsed laser sources though. It is not likely to make pulsed laser sources more attractive because the higher intensities they afford are still not practical in fibers.

Recently Brenci et al. (Ref. 39) demonstrated the transmission of argon ion laser radiation, like that being considered for this application, up to 18 Watts through a fiber as small as 150 microns with measured power transmission of approximately 60 percent. These levels should be adequate for SSME Raman backscatter diagnostics. Tests at UTRC confirmed the measurements for a low power, 0.7 W, argon laser operating on the 4880 A line. These measurements support the theoretical estimates described above. Further tests would be required to confirm the limitations of particular fibers.

Spectrograph/detector

The use of the optical fiber in the transportation of the collected Raman signal requires some consideration in the design of the spectrograph. The spontaneous Raman radiation collected by the optical head, and focused into the optical fiber, being incoherent, would emanate from the fiber at the characteristic numerical aperture of the fiber. Typical fibers have a numerical aperture of 0.2 to 0.4 corresponding to f-numbers from 2.5 to 1.25. This is faster than most fast general purpose spectrographs which are typically f/8. Recently however some spectrographs have been designed employing concave gratings which are f/4. The fiber being envisioned for this application is a 50 micron core graded-index fiber with a numerical aperture of 0.14. This nominally requires a f/3.5 spectrometer. A spectrograph has been designed for use in CARS tests at UTRC which is f/3.5, employing a 20 cm diameter concave holographic grating with a groove spacing corresponding to 2000 grooves per mm. This particular instrument with this grating has a dispersion of 5 A/mm.

The required spectral dispersion depends on the Raman transitions being observed. A larger spectral working range is needed for rotational Raman scattering than for vibrational Q-branch diagnostics. The scattered wavelengths corresponding to rotational transitions span 285 Angstroms, from 4965 to 5250 A for 4880 A laser excitation for the SSME gas conditions. In order to disperse this spectrum across an optical multichannel detector face of 25 mm requires a dispersion of 11 A/mm. However one may choose to disperse over half the active

area to avoid edge effects so that a dispersion of 25 A/mm may be preferred. This dispersion can be achieved by proper selection of the grating groove spacing. The vibrational hydrogen Q-branch spans a wavelength range from 6123 A to 6063 A for 4880 A excitation. This would require a dispersion of 5 A/mm to disperse the spectrum across half the detector face.

For unit magnification in the spectrometer, a 50 micron fiber coupled directly into the entrance would limit the resolution to two 25 micron wide pixels on the detector. Since the dispersion optimized for rotational Raman corresponds to 0.1 cm^{-1} per micron, the instrumental spectral resolution would be 5 cm^{-1}. With some defocusing, which is characteristic of diode arrays, this resolution may be degraded to 8 cm^{-1}. The spectral resolution for vibrational Raman diagnostics would be higher.

The detector envisaged for this application is a self scanning diode array. This detector has good optical response at the wavelength of use, corresponding to 0.2 counts per photon. Each detector element or pixel can be individually accessed, processed and converted in 16 microseconds. Unwanted pixels can be bypassed at 0.5 microseconds/pixel. Therefore a spectrum consisting of 6 or 7 lines can be scanned in 2 milliseconds when allowance is made for reading 10 pixels around the Raman lines. The diode array is much less sensitive to vibration than a vidicon detector, and does not suffer from blooming. The detector does have a limited dynamic range requiring care not to saturate the detector. This limits the dynamic range for one scan to 2000 counts.

Figure 7 depicts the design of the spectrograph. This is similar to the spectrograph used for CARS measurements. A fiber transmits the collected radiation to the entrance of the spectrometer where a prism may be used to afford access to the grating entrance pupil. The light from the turning prism diverges to fill the concave grating which refocuses and diperses it on the face of the diode array. The grating is designed to work slightly off axis as shown, and produce a flat field. Minimum grating tuning is generally required, dispensing with the need for a sine bar and precision lead screw. The Raman spectrum dispersed on the diode is illustrated in the top of the figure.

Laser Selection

The optimum laser for Raman diagnostic is determined by the optical properties of the fiber, the response of the detector at the Raman shifted wavelength and the characteristics of Raman scattering. Raman scattering, as can be seen from Eq. (5), depends on the Stokes frequency to the fourth power, favoring the use of short wavelength lasers. The response of the detector is relatively insensitive in the range of 5000 to 8000 Angstroms falling substantially for wavelengths outside this range. The fiber critical power for the feedback

FIG. 7

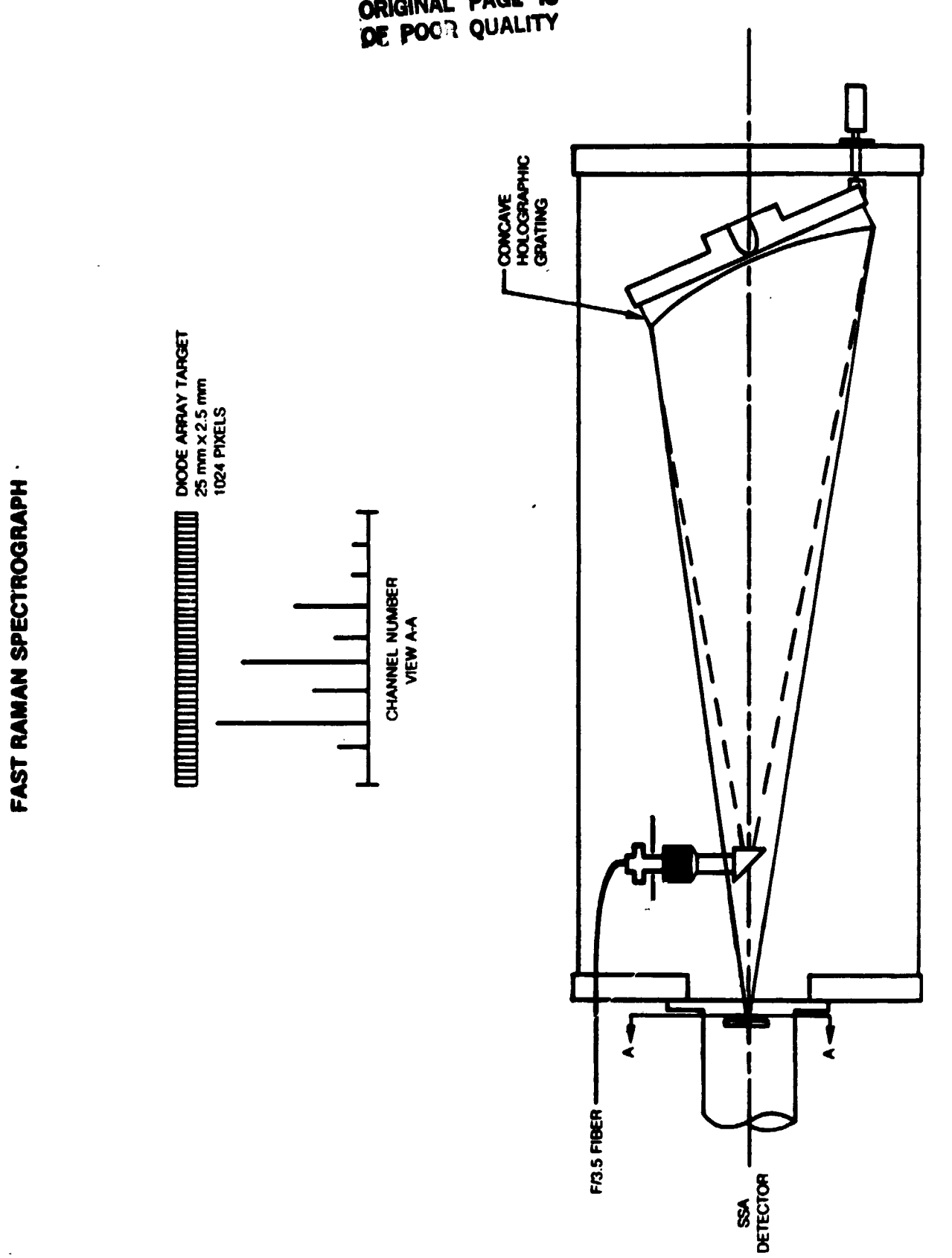

limited case increases for wavelengths less than about 4500 A, however the fraction of the radiation transmitted decreases due to the fiber attenuation. The argon ion laser seems to be a good choice, with the 4880 line being favored over the 5145 A line.

Optical Head Design

The optical head is conceived to be bolted to the SSME pre-burner. It would serve to focus light from the laser into the combustor and to collect the Raman backscattered radiation and send it to the spectrometer/detector. The optical head design concept is shown in Fig. 8. Beyond the window in the combustor are the actual elements of the optical head represented schematically. First is a device to slew the line of measurement across a segment in the chamber. This device is shown represented by a series of optical wedges mounted on a wheel which successively indexes wedges of different angular deviation into the optical path. The wedge wheel is rotated by a stepper motor. The next optical element is the combined focusing and collecting lens. This is represented as a single element but may contain a set of optical elements. Following this lens is a thick glass filter which is shown also holding a prism used to direct laser radiation to the focusing lens. The glass filter is used to block unshifted laser radiation from the collection system. A central obscuration disk also may be incorporated into this filter. Individual lenses are shown collimating the incident laser radiation and focusing the Raman radiation into the optical fiber. Finally shown are holders which provide adjustment of the optical fibers for alignment.

The possible angles that the measurement axis can be slewed through are limited by optical access into the combustor. A relatively thick window would be required to contain the pressure. This sets the distance that the slewing device must be back from the pre-burner. Off-axis scanning may be restricted by this to approximately 5 degrees, before vignetting at the window severely decreases the Raman signal.

The central obscuration disk is used to determine the spatial resolution of the coaxial system (Ref. 40). The actual resolution for a given obscuration diameter is best determined empirically. The effect of the blockage is not expected to be too severe because of the large area of the off-axis annulus.

The laser beam is shown as a small diameter pencil of light inserted into the center of the optics by a small turning prism. The laser beam can be focused into the fiber by a relatively long lens, resulting in a small solid angle entering the fiber. This small solid angle is preserved if the fiber undergoes

FIG. 8

ORIGINAL PAGE IS
OF POOR QUALITY

OPTICAL HEAD CONCEPTUAL DESIGN

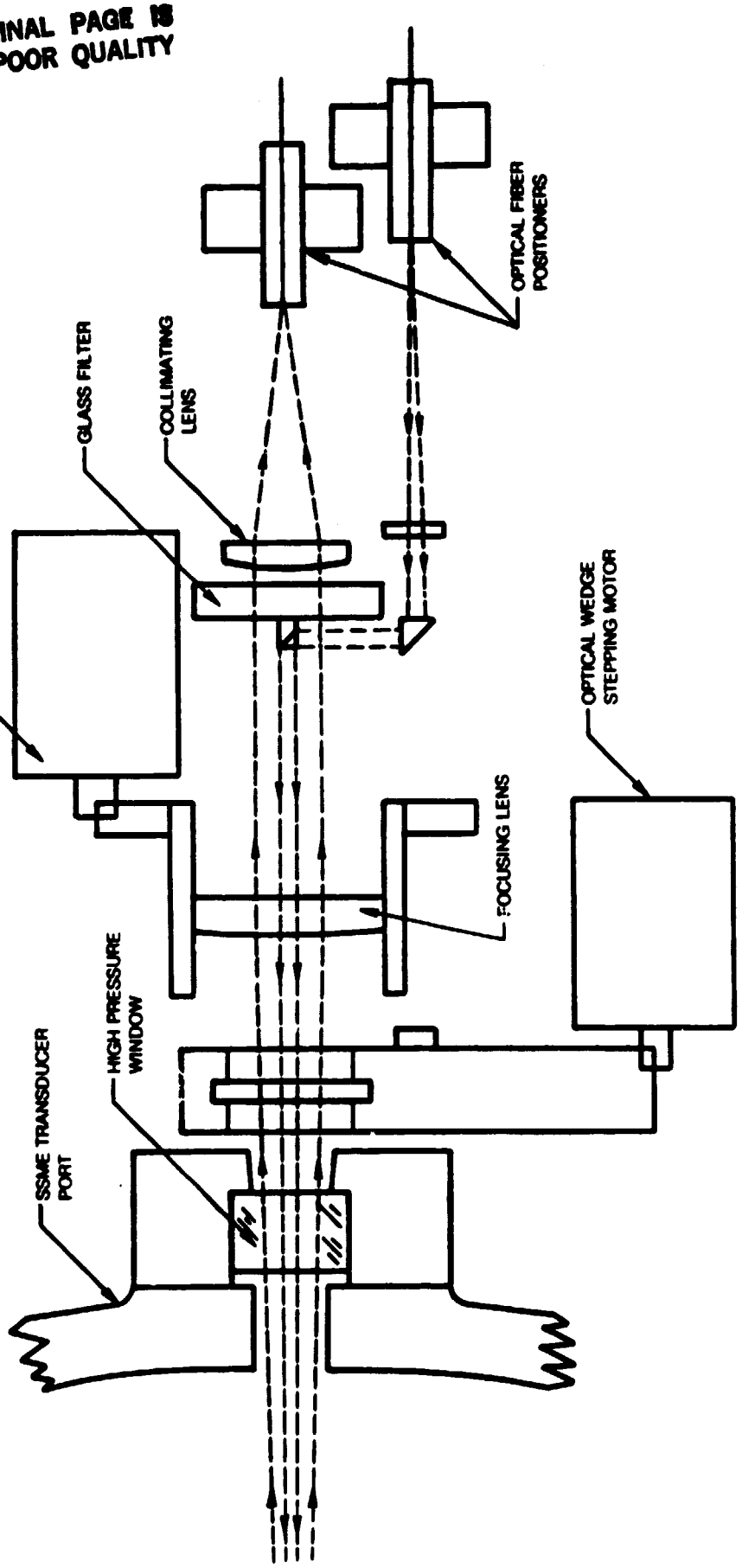

83-6-129-5

very gradual bends in transit to the optical head so the radiation travels through the fiber in low order modes. If there many microbends the low order modes couple to higher order mode which diffract more on exiting the fiber.

Raman Backscattering System Estimated Performance

Raman Signal Levels

The performance of Raman temperature diagnostic system can be measured in terms of the performance criteria or design objectives. These specify a spatial resolution of 0.5 to 1 cm, time response of 10 milliseconds, and a temperature measurement accuracy of 10 R, or 6 K. The performance of a Raman system can be estimated from the calculations of the normalized Raman intensities and the estimates of laser power that can be transmitted through the optical fiber. The estimates are also subject to the constraints imposed by the optical access in the SSME pre-burner. The transducer port is 1.1 cm in diameter and the combustion chamber is about 25 cm in diameter. Taking an optical aperture of 1 cm and a depth of 20 cm, the solid angle over which Raman backscatter can be collected is .002 steradians. The number of photoelectrons counted in the optical multichannel detector is given by

$$N_R^e = \frac{P_L \ell I_R t \epsilon_c \eta_Q}{hck_s} \qquad (30)$$

where P_R is the incident laser power, ℓ is the spatial extent of collection, i.e. the resolution, I_L is the normalized Raman intensity per cm per steradian, t is the temporal resolution, ϵ_c is the collection efficiency, η_Q is the quantum efficiency of the optical detector and k_s is the Stokes photon frequency in wavenumbers. The factors in the denominator give the energy per Stokes photon. This equation is used to estimate the number of photoelectrons counted due to a single rotational Raman transition. The collection efficiency is the resultant of all Fresnel reflection losses and transmission losses in the Raman system. The transmission for the fiber would be about 85 percent for a fiber 40 m long and having an attenuation of 20 dB/km at 5000 Å. For temperatures in the range of 1000 to 1600 K the calculated normalized Raman intensity is 2×10^{-9} to 2.3×10^{-10} $cm^{-1}sR^{-1}$ for transitions involving the lowest six rotational levels which are most populated. Taking the collection efficiency and the quantum efficiency each to be 0.2 then Eq. (30) can be expressed as

$$N_R^e = 6 \times 10^4 \frac{cm^{-1}}{J} \cdot P_L \ell t \qquad (31)$$

With an incident laser power of 4 Watts, and a spatial resolution, l = 1 cm, then the number of OMD counts is $2.4 \times 10^{+5}$ t.

The diode array was estimated to be capable of being scanned in 4.5 ms. In this period the signal would be about 1000 counts. This is within the linear range of the detector. The acquired counts from previous diode scans can be added to effectively average over a longer period of time, decreasing the temporal resolution.

Temperature Resolution

An estimate of the number of signal counts required to achieve the temperature resolution objective can be made from the expression for the rotational populations. It can be shown that the temperature resolution is given by

$$dT = T \left(\frac{kT}{hck_R}\right) \frac{dn_{vJ}}{n_{vJ}} \qquad (32)$$

where n_{vJ} is the population of the level corresponding to the quantum numbers v and J. The photon count is directly proportional to the populations n_{vJ}, therefore the populations in this expression can be taken to be the signal count as well. A 6°K temperature resolution requires a signal-to-noise ratio of 120. For shot noise limited statistics then the required number of photon counts is 15000, which according to the estimate above would require 63 msec, or somewhat longer than the design 10 msec. This estimate is based on the least populated rotational level. The highest populated level can be nearly an order of magnitude higher, for which the temporal resolution criterion would be satisfied. In actual analysis, the temperature would be obtained from the distribution of Raman intensity, therefore the temporal resolution would be expected to fall in between these two limits. If tests indicate that more power can be propagated through the fiber then the temperature resolution can be correspondingly higher.

Potential Background Interferences

These estimates give the expected signal level in absolute terms. It is also important to examine the Raman system performance with respect to background interferences. No optical measurements have been done in the SSME pre-burner, therefore the radiation background can only be estimated.

Hydrogen and oxygen burn with a flame of very low visible luminosity. Therefore the most important background interference to Raman measurements is likely to be thermal radiation from either particles in the flow, such as from erosion, or from hot surfaces adjacent to the flow. In normal operation both of

these sources would be expected to be quite low. To determine the relative magnitude of thermal background for conditions likely to obtain in the SSME pre-burner estimates of the possible particle loadings have been made. The model is a mono-disperse distribution of particles of diameter d, with a number density of n.

Hottel and Sarofim (Ref. 41) derived an expression for the thermal radiation from a collection of particles, by relating the emissivity to the absorptivity. They showed that the emissivity ϵ, is given by

$$\epsilon = 1 - \exp(-c a \ell) \qquad (33)$$

where c is the concentration of particles, a is the absorption area of the particles and ℓ is the optical path length. For a number density of 10^4 particles per cm^3, having a mean diameter of 10 microns and a path length of 25 cm, the emissivity is calculated to be 0.28. For particles at a temperature of 1000 K the calculated grey body emission intensity is 5×10^{-11} watts/cm^{-1} cm^{-2} sR^{-1}. It should be noted that this particle loading corresponds to a high rate of erosion (70 gm/sec for a metal of density 4.5 gm/cm^3 such as titanium), and it is quite likely that this level of erosion would be detected in some other manner and the test terminated.

The thermal radiation intensity is a strong function of particle temperature, whereas Raman scattering is much less sensitive to gas temperature. This is shown in Fig. 9 which shows the calculated spectral irradiance for Raman scattering with 10^4 Watt/cm^2 incident laser intensity and the calculated thermal emission for two emissivities as a function of temperature. The Raman irradiance is calculated to exceed the thermal radiation for most particle loading at temperatures below 1500°K, therefore the thermal radiation from particles is not expected under normal operation to be an impediment to Raman measurements.

The pre-burner walls would have a larger emissivity than a collection of particles, but the temperature is expected to be considerably lower. The strong temperature coefficient implies that the radiation from the wall would also be expected to be low compared to the Raman scattered radiation.

COMPARISON OF PREDICTED RAMAN AND THERMAL RADIATION IRRADIANCES

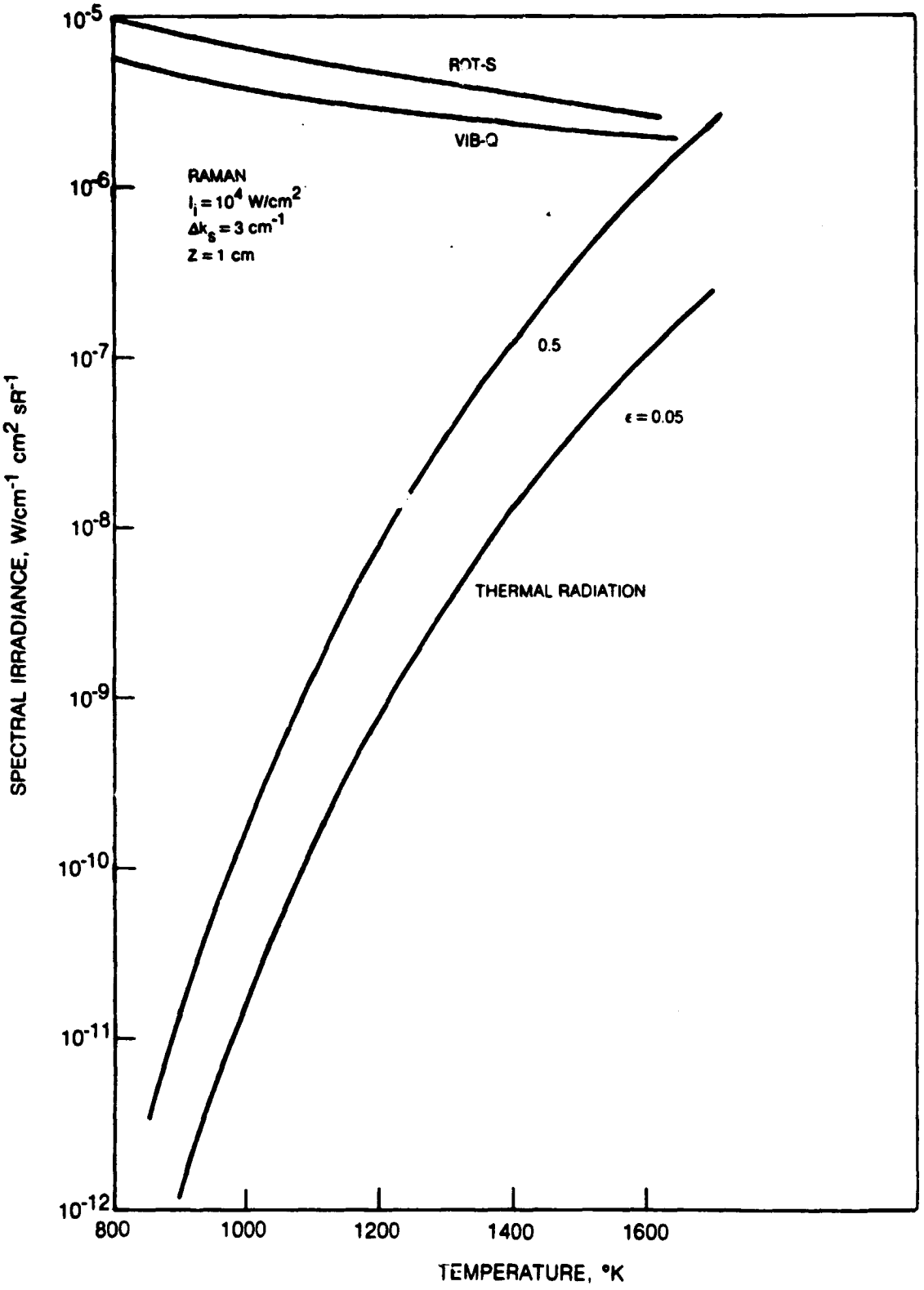

83-5-129-4

CONCLUSIONS

The feasibility of remote optical diagnostics in the space shuttle main engine fuel pre-burner has been investigated. Diagnostics based on Raman backscattering appear to be the superior technique for the medium, offering advantages over fluorescence and coherent nonlinear techniques, such as CARS. No seed or additive species and no modifications to the pre-burner are needed. Raman diagnostics appear to be amenable to implementation with optical fibers, which is required by the constraints of operating in the environment of a high performance rocket engine.

The use of Raman backscattering, based on theoretical predictions, appears to have a reasonable chance of meeting diagnostic system design goals. Again based on calculations, it appears feasible to transmit 5 to 10 Watts of argon laser radiation through a multimode optical fiber 50 to 100 microns in diameter to excite the Raman radiation. This level is predicted to be sufficient to achieve the program design goals of 6 K temperature resolution, 1 cm spatial resolution and 10 milliseconds temporal resolution. Some tradeoffs may be required when the effect of obscuration, needed to achieve the requisite spatial resolution in the coaxial geometry, is taken into account. This effect is difficult to quantify theoretically in simple terms. Obscuration also may sharply affect off-axis temperature measurements, requiring relaxation of the design goals. The difficulties normally associated with Raman scattering: weak signal strength and interference due to background radiation are not expected to be problematic due to the very high density in this application, and the low flame luminosity expected in the fuel-rich hydrogen-oxygen flame. There appear to be no theoretical hurdles or difficulties to analyzing Raman spectra.

Potential problems which are difficult to quantify in a paper study pertain to the optical quality of the high pressure combustion medium. There are no measurements of the optical quality of the flow. Strong density gradients due to mixing, combustion pressure waves, and two phase flow in the propellant spray could pose severe problems. In the worst case, these effects could make it impossible to determine the precise point of measurement, or if severe enough, prevent collection of the backscattered radiation. On the other hand, the dominant species in the flow, hydrogen, has a very low Gladstone-Dale constant so that at this pressure this medium is more suitable than others. In addition Raman scattering, being an incoherent technique, should suffer least from medium optical problems. Hot gas tests are need to assess the magnitude of these difficulties. The design of the window is expected to present a challenge. The window must provide a safe, positive seal of the combustion chamber, at the same time withstanding thermal shock, and the radiation heat load from the combustor.

REFERENCES

1. A. C. Eckbreth, P. A. Bonczyk and J. F. Verdieck, "Combustion Diagnostics by Laser Raman and Fluorescence Techniques", Prog. Energy and Combustion Science, Vol. 5, pp. 253-322, 1979.

2. B. T. Zinn, ed., Experimental Diagnostics in Gas Phase Systems, Vol. 53, Progress in Astronautics and Aeronautics, Amer. Inst. Aeronautics and Astronautics, New York, 1977.

3. D. R. Crosley, Laser Probes for Combustion Chemistry, ACS Symposium Series 134, American Chemical Society, Wash. D.C., 1980.

4. A. C. Eckbreth, "Recent Advances in Laser Diagnostics for Temperature and Species Concentrations in Combustion", 18th Symp. (Intl.) on Combustion, The Combustion Inst., 1981.

5. M. Lapp and C. M. Penney, eds., Laser Raman Gas Diagnostics, Plenum Press, New York, 1974.

6. M. C. Drake, C. Asawaroengchai, D. L. Drapcho, K. D. Veirs and G. M. Rosenblatt, The Use of Rotational Raman Scattering for Measurements of Gas Temperature", in Temperature, J. F. Schooley, ed., American Inst. of Physics, 1982, pp. 621-629.

7. M. C. Drake, M. Lapp and C. M. Penney, "Use of the Vibrational Raman Effect for Gas Temperature Measurements", in Temperature, J. F. Schooley, ed., American Inst. of Physics, 1982, pp. 631-638.

8. J. W. Nibler, W. M. Shaub, J. R. McDonald and A. B. Harvey, "Coherent Anti-Stokes Raman Spectroscopy", in Vibrational Spectra and Structure, Vol. 6, J. R. Durig, ed., Elsevier, Amsterdam, 1977.

9. A. B. Harvey, ed., Chemical Applications of Nonlinear Spectroscopy, Academic Press, New York, 1981.

10. G. L. Eesley, Coherent Raman Spectroscopy, Pergamon Press, Oxford, 1981.

11. M. D. Levenson, Introduction to Nonlinear Laser Spectroscopy, Academic Press, New York, 1982.

REFERENCES (Cont'd)

12. J. M. Cherlow and S. P. S. Porto, "Laser Raman Spectroscopy of Gases", in Laser Spectroscopy of Atoms and Molecules, H. Walther, ed., Springer-Verlag, 1976.

13. S. N. Suchard, ed., Spectroscopic Data Vol. 1 - Hetereonuclear Diatomic Molecules, Plenum, New York, 1975.

14. R. P. Lucht, D. W. Sweeney and N. M. Laurendeau, "Laser-Saturated Fluorescence Measurements of OH Concentration in Flames", Comb. and Flame Vol. 50, pp. 189-205, 1983.

15. T. C. James and W. Klemperer, "Line Intensities in the Raman Effect of $^1\Sigma$ Diatomic Molecules", J. Chem. Phys., Vol. 31, pp. 130-134, 1959.

16. C. Asawaroengchai and G. M. Rosenblatt, "Rotational Raman Intensities and the Measured Change with Internuclear Distance of the Polarizability Anisotropy of H_2, D_2, N_2, O_2, and CO", J. Chem. Phys., Vol. 72, pp. 2664-2669, 1980.

17. L. M. Cheung, D. M. Bishop, D. L. Drapcho and G. M. Rosenblatt, "Relative Raman Line Intensities for H_2 and for D_2. Correction Factors for Molecular Non-Rigidity", Chem. Phys. Letters, Vol. 80, pp. 445-450, 1981.

18. W. F. Murphy, W. Holzer and H. J. Bernstein, "Gas Phase Raman Intensities: A Review of Pre-Laser Data", Appl. Spectrosc., Vol. 23, pp. 211-218, 1969.

19. R. P. Srivastava and H. R. Zaidi, "Intermolecular Forces Revealed by Raman Scattering", Chap 5 in Raman Spectroscopy, A. Weber, ed., Springer-Verlag, Berlin, 1979.

20. R. H. Dicke, "The Effect of Collisions Upon the Doppler Width of Spectral Lines", Phys. Rev., Vol. 89, pp. 472-473, 1953.

21. E. D. Hinkley, K. W. Nill, and F. A. Blum, "Infrared Spectroscopy with Tunable Lasers", Ch. 2 in Laser Spectroscopy of Atoms and Molecules, H. Walther, ed., Springer-Verlag, Berlin, 1976.

22. P. Dion and A. D. May, "Motional Narrowing and Other Effects in the Q Branch of HD", Can. J. Phys., Vol. 51, pp. 36-39, 1973.

REFERENCES (Cont'd)

23. P. Lallemand and P. Simova, "Stimulated Raman Spectroscopy in Hydrogen Gas", J. Mol. Spec., Vol. 26, pp. 262-276, 1968.

24. R. A. J. Keijser, J. R. Lombardi, K. D. Van Den Hout, B. C. Sanctuary and H. F. P. Knapp, "The Pressure Broadening of the Rotational Raman Lines of Hydrogen Isotopes", Physica, Vol. 76, pp. 585-608, 1974.

25. V. G. Cooper, A. D. May, E. H. Hara, and H. F. P. Knapp, "Dicke Narrowing and Collisional Broadening of the $S_0(0)$ and $S_0(1)$ Raman Line of H_2", Can. J. Phys., Vol. 46, pp. 2019-2023, 1968.

26. A. D. May, V. Degen, J. C. Stryland and H. L. Welsh, "The Raman Effect in Gaseous Hydrogen at High Pressures", Can. J. Phys., Vol. 39, pp. 1769-1783, 1961.

27. E. Allin, A. D. May, B. P. Stoicheff, J. C. Stryland and H. L. Welsh, "Spectroscopy Research at the McLennan Physical Laboratories of the University of Toronto", Appl. Optics, Vol. 6, pp. 1597-1608, 1967.

28. J. R. Murray and A. Javan, "Motional Narrowing in Hydrogen Raman Scattering", J. Molec. Spect., Vol. 29, pp. 502-504, 1969.

29. R. D. McCarty, Hydrogen: Its Technology and Implications, Vol. III Hydrogen Properties, CRC Press, Cleveland, OH, 1978.

30. G. Herzberg, Spectra of Diatomic Molecules, D. Van Nostrand, Princeton, NJ, 1950.

31. A. Farkas and L. Farkas, Proc. Roy. Soc. (London), Vol. A162, pp. 124, 1935.

32. G. Boato, G. Careri, A. Ciminao, E. Molinari and G. G. Volpi, "Homogeneous Exchange Reaction between Hydrogen and Deuterium", J. Chem. Phys., Vol. 24, pp. 783-791, 1956.

33. G. Hammes, Principles of Chemical Kinetics, Academic Press, New York, 1978.

34. M. Karplus, R. N. Porter and R. D. Sharma, "Exchange Reactions with Activation Energy. I. Simple Barrier Potential for (H, H_2)", J. Chem. Phys., Vol. 43, pp. 3259-3287, 1965.

REFERENCES (Cont'd)

35. R. G. Smith, "Optical Power Handling Capacity of Low Loss Optical Fibers as Determined by Stimulated Raman and Brillioun Scattering", Appl. Optics, Vol. 11, pp. 2409-2494, 1972.

36. J. E. Midwinter, Optical Fibers for Transmission, J. Wiley & Sons, New York, 1979.

37. R. H. Stolen, "Nonlinear Properties of Optical Fibers", in Optical Fiber Telecommunications, S. E. Miller and A. G. Chynoweth, eds., Academic Press, New York, 1979.

38. P. Labudde, P. Anliker and H. P. Weber, "Transmission of Narrow Band High Power Laser Radiation through Optical Fibers", Optics Commun., Vol. 32, pp. 385-390, 1980.

39. M. Brenci, R. Falciai, M. Mazzoni and A. M. Scheggi, "Variable Section Optical-Fiber Delivery System of High-Power Laser Radiation for Surgical Use", Appl. Optics, Vol. 22, pp. 373-375, 1983.

40. A. C. Eckbreth and J. W. Davis, "Spatial Resolution Enhancement in Coaxial Light Scattering Geometries", Appl. Optics, Vol. 16, pp. 804-806, 1977.

41. H. C. Hottel and A. F. Sarofim, Radiative Transfer, McGraw-Hill, New York, 1967.

APPENDIX A

The calculated Raman frequencies and intensities are tabulated in this appendix. The molecular parameters give the energy level constants, spin statistical weights, molecular polarizability and incident laser frequency. These constants can be changed to reflect a new set of energy constants, or updated polarizabilities. The term values, referred to zero in the lowest rotational level of the v = 0 state, are tabulated next. The Raman shift is calculated from the difference in these values. The frequency shifts, and wavelength for the assumed pump frequency are shown next for the v = 0 level for rotational transitions, and v = 0 --> 1 vibrational-rotational transitions. Lastly the populations and Raman intensities for the various Raman branches are tabulated. The populations are in units of cm^{-3}, and the intensities are $cm^{-1}sR^{-1}$. Energies and frequencies are in cm^{-1}, and wavelengths are in Angstroms.

%

HYDROGEN

Molecular Parameters

4401.213	121.3340	0.0129000	0.0000000E+00
60.85300	3.062200	5.7700001E-02	5.1000002E-03
4.7100000E-02	2.7399999E-03	3.9999999E-04	
4.8999998E-05	4.9999997E-06		
0.2500000	0.7500000		

0.3140E-24 0.3800 0.1230E-15 0.1020E-15 0.7410E-08

Laser Frequency = 20472.00 cm-1

Zero Point Term Value Matrix

V=0	V=1	V=2	V=3	V=4	J
0.0000000E+00	4161.183	8087.010	11702.36	15252.11	0
118.4885	4273.752	8193.796	11803.44	15347.49	1
354.3743	4497.846	8406.350	12004.58	15537.23	2
705.5090	4831.402	8722.658	12303.79	15819.30	3
1168.754	5271.405	9139.771	12778.12	16190.71	4
1740.079	5813.972	9653.874	13263.74	16647.54	5
2414.700	6454.473	10260.40	13836.07	17185.07	6
3187.242	7187.683	10954.15	14487.81	17797.82	7
4051.943	8007.955	11729.47	15219.15	18479.69	8
5002.887	8909.437	12580.40	16017.91	19224.09	9
6034.274	9886.305	13500.94	16879.71	20024.10	10
7140.717	10933.04	14485.24	17798.15	20872.63	11
8317.582	12044.71	15527.85	18767.12	21762.61	12
9561.350	13217.32	16624.08	19780.94	22687.22	13
10870.03	14448.15	17770.24	20834.73	23640.08	14
12243.57	15736.17	18964.01	21924.63	24615.56	15
13684.37	17082.43	20204.84	23048.17	25608.98	16
15197.73	18490.51	21494.29	24204.59	26616.93	17
16792.43	19967.04	22836.49	25395.19	27637.57	18
18481.26	21522.14	24238.55	26623.74	28670.97	19
20281.67	23170.01	25711.07	27896.86	29719.43	20
22216.37	24929.50	27268.63	29224.49	30787.84	21
24314.00	26824.66	28930.29	30620.31	31884.09	22
26609.86	28885.40	30720.19	32102.21	33019.45	23
29146.61	31148.18	32668.08	33692.84	34208.98	24
31975.08	33656.60	34807.93	35420.07	35472.01	25
35155.05	36462.24	37188.62	37317.59	36832.54	26
38756.06	39625.31	39854.51	39425.41	38319.76	27

Raman Frequency Shifts

J	Rot-O	Rot-S	Vib-O	Vib-Q	Vib-S
0	0.00	354.37	0.00	4161.18	4497.05
1	0.00	587.02	0.00	4155.26	4712.91
2	-354.37	814.38	3806.81	4143.47	4917.03
3	-587.02	1034.57	3568.24	4125.89	5108.46
4	-814.38	1245.95	3329.09	4102.65	5285.72
5	-1034.57	1447.16	3091.32	4073.89	5447.60
6	-1245.95	1637.24	2856.71	4039.77	5593.25
7	-1447.16	1815.65	2626.73	4000.44	5722.19
8	-1637.24	1982.33	2402.53	3956.01	5834.36
9	-1815.65	2137.83	2184.80	3906.55	5930.15
10	-1982.33	2283.31	1973.68	3852.03	6010.43
11	-2137.83	2420.63	1768.72	3792.32	6076.60
12	-2283.31	2552.45	1568.72	3727.13	6130.57
13	-2420.63	2682.22	1371.69	3655.97	6174.82
14	-2552.45	2814.34	1174.68	3578.13	6212.40
15	-2682.22	2954.16	973.74	3492.59	6246.94

16	-2814.34	3108.05	763.70	3398.05	6282.67
17	-2954.16	3283.53	538.44	3292.78	6324.41
18	-3108.05	3489.24	290.00	3174.61	6377.59
19	-3283.53	3735.11	9.25	3040.88	6448.24
20	-3489.24	4032.33	-314.63	2880.34	6542.99
21	-3735.11	4393.49	-694.23	2713.13	6669.04
22	-4032.33	4832.61	-1143.99	2510.65	6834.18
23	-4393.49	5365.23	-1680.36	2275.55	7046.74
24	-4832.61	6008.44	-2321.96	2001.57	7315.63
25	-5365.23	6780.97	-3089.68	1681.52	7650.22

Raman Wavelengths

	Rotational		Vibrational		
J	Lamda-O	Lamda-S	Lamda-O	Lamda-Q	Lamda-S
0	0.00	4965.83	0.00	6123.39	6252.28
1	0.00	5023.87	0.00	6121.17	6337.50
2	4797.00	5081.92	5993.34	6116.76	6420.56
3	4744.05	5139.42	5908.05	6110.19	6500.46
4	4693.43	5195.87	5826.52	6101.52	6576.23
5	4645.42	5250.77	5748.90	6090.84	6646.99
6	4600.25	5303.70	5675.45	6078.20	6711.97
7	4558.06	5354.36	5597.45	6063.71	6770.57
8	4518.91	5402.58	5528.08	6047.42	6822.38
9	4482.77	5448.35	5462.33	6029.38	6867.26
10	4449.52	5491.88	5400.06	6009.63	6905.33
11	4418.95	5533.62	5340.94	5988.14	6937.03
12	4390.72	5574.27	5284.50	5964.85	6963.10
13	4364.40	5614.89	5230.04	5939.64	6984.62
14	4339.44	5656.86	5176.70	5912.31	7003.00
15	4315.14	5701.95	5123.41	5882.56	7019.98
16	4290.68	5752.43	5068.88	5850.02	7037.63
17	4265.09	5811.09	5011.64	5814.22	7058.36
18	4237.28	5881.40	4950.00	5774.54	7084.96
19	4206.00	5967.69	4882.16	5730.29	7120.60
20	4169.93	6075.46	4806.16	5680.64	7168.97
21	4127.61	6211.75	4720.05	5624.65	7234.34
22	4077.58	6385.94	4621.93	5561.32	7321.81
23	4018.41	6610.79	4510.12	5489.54	7437.57
24	3948.73	6904.38	4383.28	5408.20	7589.34
25	3867.39	7293.40	4240.58	5316.18	7787.09

Pressure = 5500.00000 psia

Temp = 300 Qrot = 1.8882 Qvib = 1.0000

		Rotational		Vibrational		
J	N(J)	I(O-branch)	I(S-branch)	I(O-branch)	I(Q-branch)	I(S-branch
0	1.212E+21	0.000E+00	4.823E-09	0.000E+00	1.543E-09	1.333E-10
1	6.086E+21	0.000E+00	1.409E-08	0.000E+00	8.073E-09	3.462E-10
2	1.052E+21	9.613E-10	2.042E-09	3.506E-11	1.377E-09	4.397E-11
3	7.670E+20	9.572E-10	1.359E-09	3.737E-11	9.992E-10	2.532E-11
4	3.183E+19	4.717E-11	5.356E-11	1.949E-12	4.129E-11	8.497E-13
5	6.304E+18	1.065E-11	1.031E-11	4.606E-13	8.137E-12	1.372E-13

Temp = 400 Qrot = 2.4503 Qvib = 1.0000

		Rotational		Vibrational		
J	N(J)	I(O-branch)	I(S-branch)	I(O-branch)	I(Q-branch)	I(S-branch
0	6.983E+20	0.000E+00	2.778E-09	0.000E+00	8.890E-10	7.681E-11
1	4.056E+21	0.000E+00	9.392E-09	0.000E+00	5.381E-09	2.308E-10
2	9.389E+20	8.579E-10	1.822E-09	3.129E-11	1.229E-09	3.926E-11
3	1.060E+21	1.323E-09	1.879E-09	5.166E-11	1.382E-09	3.501E-11
4	7.889E+19	1.169E-10	1.327E-10	4.830E-12	1.023E-10	2.106E-12
5	3.241E+19	5.476E-11	5.301E-11	2.368E-12	4.183E-11	7.053E-13
6	9.23[illegible]E+17	1.750E-12	1.493E-12	7.842E-14	1.185E-12	1.638E-14

Temp = 500 Qrot = 3.0280 Qvib = 1.0000

		Rotational		Vibrational		
J	N(J)	I(O-branch)	I(S-branch)	I(O-branch)	I(Q-branch)	I(S-branch
0	4.535E+20	0.000E+00	1.804E-09	0.000E+00	5.774E-10	4.909E-11
1	2.876E+21	0.000E+00	6.650E-09	0.000E+00	3.015E-09	1.636E-10
2	7.930E+20	7.246E-10	1.539E-09	2.643E-11	1.038E-09	3.316E-11
3	1.165E+21	1.453E-09	2.064E-09	5.674E-11	1.517E-09	3.845E-11
4	1.230E+20	1.823E-10	2.069E-10	7.530E-12	1.595E-10	3.203E-12
5	7.828E+19	1.323E-10	1.280E-10	5.719E-12	1.010E-10	1.703E-12
6	3.771E+18	7.149E-12	6.098E-12	3.203E-13	4.039E-12	6.690E-14
7	1.125E+18	2.376E-12	1.822E-12	1.092E-13	1.433E-12	1.610E-14

Temp = 600 Qrot = 3.5981 Qvib = 1.0000

		Rotational		Vibrational		
J	N(J)	I(O-branch)	I(S-branch)	I(O-branch)	I(Q-branch)	I(S-branch
0	3.180E+20	0.000E+00	1.265E-09	0.000E+00	4.049E-10	3.499E-11
1	2.138E+21	0.000E+00	4.950E-09	0.000E+00	2.836E-09	1.216E-10
2	6.625E+20	6.054E-10	1.286E-09	2.200E-11	8.671E-10	2.770E-11
3	1.159E+21	1.447E-09	2.055E-09	5.648E-11	1.510E-09	3.827E-11
4	1.546E+20	2.291E-10	2.601E-10	9.466E-12	2.006E-10	4.127E-12
5	1.318E+20	2.226E-10	2.155E-10	9.627E-12	1.701E-10	2.867E-12
6	9.010E+18	1.700E-11	1.457E-11	7.651E-13	1.156E-11	1.590E-13
7	4.043E+18	8.540E-12	6.551E-12	3.925E-13	5.151E-12	5.818E-14
8	1.479E+17	3.470E-13	2.428E-13	1.621E-14	1.869E-13	1.710E-15

Temp = 700 Qrot = 4.1683 Qvib = 1.0002

		Rotational		Vibrational		
J	N(J)	I(O-branch)	I(S-branch)	I(O-branch)	I(Q-branch)	I(S-branch
0	2.353E+20	0.000E+00	9.361E-10	0.000E+00	2.996E-10	2.588E-11
1	1.649E+21	0.000E+00	3.810E-09	0.000E+00	2.107E-09	9.301E-11
2	5.554E+20	5.075E-10	1.078E-09	1.851E-11	7.269E-10	2.323E-11
3	1.101E+21	1.374E-09	1.952E-09	5.366E-11	1.435E-09	3.636E-11
4	1.735E+20	2.572E-10	2.720E-10	1.063E-11	2.251E-10	4.633E-12
5	1.822E+20	3.078E-10	2.979E-10	1.331E-11	2.351E-10	3.964E-12
6	1.600E+17	3.033E-11	2.587E-11	1.359E-12	2.053E-11	2.833E-13
7	9.612E+18	2.030E-11	1.557E-11	9.331E-13	1.225E-11	1.383E-13
8	4.908E+17	1.152E-12	8.857E-13	5.381E-14	6.201E-13	5.674E-15

Temp = 800 Qrot = 4.7389 Qvib = 1.0006

		Rotational		Vibrational		
J	N(J)	I(O-branch)	I(S-branch)	I(O-branch)	I(Q-branch)	I(S-branch
0	1.810E+20	0.000E+00	7.202E-10	0.000E+00	2.305E-10	1.991E-11
1	1.309E+21	0.000E+00	3.030E-09	0.000E+00	1.736E-09	7.447E-11
2	4.693E+20	4.289E-10	9.107E-10	1.544E-11	6.143E-10	1.963E-11
3	1.022E+21	1.276E-09	1.812E-09	4.980E-11	1.332E-09	3.374E-11
4	1.825E+20	2.705E-10	3.071E-10	1.118E-11	2.360E-10	4.872E-12
5	2.240E+20	3.785E-10	3.664E-10	1.637E-11	2.892E-10	4.875E-12
6	2.373E+19	4.499E-11	3.830E-11	2.016E-12	3.045E-11	4.210E-13
7	1.775E+19	3.749E-11	2.876E-11	1.723E-12	2.261E-11	2.554E-13
8	1.164E+18	2.731E-12	1.911E-12	1.276E-13	1.471E-12	1.346E-14
9	5.443E+17	1.417E-12	9.138E-13	6.673E-14	6.810E-13	4.982E-15

Temp = 900 Qrot = 5.3096 Qvib = 1.0013

		Rotational		Vibrational		
J	N(J)	I(O-branch)	I(S-branch)	I(O-branch)	I(Q-branch)	I(S-branch
0	1.435E+20	0.000E+00	5.709E-10	0.000E+00	1.827E-10	1.579E-11
1	1.063E+21	0.000E+00	2.462E-09	0.000E+00	1.410E-09	6.049E-11
2	4.002E+20	3.657E-10	7.760E-10	1.334E-11	5.238E-10	1.674E-11
3	9.377E+20	1.170E-09	1.662E-09	4.563E-11	1.222E-09	3.095E-11
4	1.845E+20	2.735E-10	3.105E-10	1.130E-11	2.394E-10	4.926E-12
5	2.558E+20	4.322E-10	4.184E-10	1.869E-11	3.302E-10	5.566E-12
6	3.136E+19	5.944E-11	5.070E-11	2.663E-12	4.023E-11	5.563E-13

7	2.780E+19	5.873E-11	4.505E-11	2.699E-12	3.542E-11	4.001E-13
8	2.215E+18	5.197E-12	3.636E-12	2.420E-13	2.798E-12	2.560E-14
9	1.289E+18	3.356E-12	2.164E-12	1.581E-13	1.613E-12	1.180E-14
10	6.786E+16	1.960E-13	1.175E-13	9.232E-15	8.396E-14	4.819E-16

Temp = 1000 Qrot = 5.8802 Qvib = 1.0025

		Rotational		Vibrational		
J	N(J)	I(O-branch)	I(S-branch)	I(O-branch)	I(Q-branch)	I(S-branch
0	1.165E+20	0.000E+00	4.634E-10	0.000E+00	1.483E-10	1.281E-11
1	8.799E+20	0.000E+00	2.037E-09	0.000E+00	1.167E-09	5.006E-11
2	3.444E+20	3.147E-10	6.684E-10	1.148E-11	4.507E-10	1.440E-11
3	8.554E+20	1.067E-09	1.516E-09	4.167E-11	1.114E-09	2.824E-11
4	1.820E+20	2.697E-10	3.062E-10	1.114E-11	2.360E-10	4.857E-12
5	2.780E+20	4.677E-10	4.546E-10	2.031E-11	3.588E-10	6.049E-12
6	3.830E+19	7.260E-11	6.192E-11	3.252E-12	4.914E-11	6.794E-13
7	3.891E+19	8.219E-11	6.304E-11	3.777E-12	4.757E-11	5.599E-13
8	3.622E+18	8.498E-12	5.945E-12	3.970E-13	4.576E-12	4.187E-14
9	2.511E+18	6.538E-12	4.216E-12	3.077E-13	3.142E-12	2.299E-14
10	1.606E+17	4.639E-13	2.700E-13	2.185E-14	1.907E-13	1.141E-15

Temp = 1100 Qrot = 6.4511 Qvib = 1.0044

		Rotational		Vibrational		
J	N(J)	I(O-branch)	I(S-branch)	I(O-branch)	I(Q-branch)	I(S-branch
0	9.634E+19	0.000E+00	3.833E-10	0.000E+00	1.227E-10	1.060E-11
1	7.395E+20	0.000E+00	1.712E-09	0.000E+00	9.809E-10	4.207E-11
2	2.988E+20	2.730E-10	5.799E-10	9.958E-12	3.911E-10	1.249E-11
3	7.784E+20	9.714E-10	1.380E-09	3.792E-11	1.014E-09	2.569E-11
4	1.765E+20	2.615E-10	2.969E-10	1.080E-11	2.289E-10	4.711E-12
5	2.919E+20	4.933E-10	4.775E-10	2.133E-11	3.768E-10	6.353E-12
6	4.425E+19	8.388E-11	7.155E-11	3.758E-12	5.670E-11	7.050E-13
7	5.026E+19	1.062E-10	8.143E-11	4.879E-12	6.403E-11	7.232E-13
8	5.313E+18	1.247E-11	8.722E-12	5.825E-13	6.713E-12	6.143E-14
9	4.252E+18	1.107E-11	7.137E-12	5.213E-13	5.320E-12	3.092E-14
10	3.188E+17	9.209E-13	5.519E-13	4.338E-14	3.945E-13	2.264E-15
11	1.818E+17	5.820E-13	3.267E-13	2.726E-14	2.221E-13	9.737E-16

Temp = 1200 Qrot = 7.0219 Qvib = 1.0069

		Rotational		Vibrational		
J	N(J)	I(O-branch)	I(S-branch)	I(O-branch)	I(Q-branch)	I(S-branch
0	8.093E+19	0.000E+00	3.220E-10	0.000E+00	1.030E-10	8.903E-12
1	6.295E+20	0.000E+00	1.457E-09	0.000E+00	8.350E-10	3.581E-11
2	2.612E+20	2.387E-10	5.067E-10	8.705E-12	3.418E-10	1.092E-11
3	7.081E+20	8.836E-10	1.255E-09	3.449E-11	9.225E-10	2.337E-11
4	1.693E+20	2.509E-10	2.848E-10	1.036E-11	2.196E-10	4.519E-12
5	2.992E+20	5.056E-10	4.894E-10	2.186E-11	3.862E-10	6.511E-12
6	4.911E+19	9.310E-11	7.941E-11	4.171E-12	6.302E-11	8.713E-13
7	6.121E+19	1.293E-10	9.918E-11	5.942E-12	7.799E-11	8.808E-13
8	7.196E+18	1.688E-11	1.181E-11	7.088E-13	9.091E-12	8.319E-14
9	6.488E+18	1.689E-11	1.009E-11	7.955E-13	8.118E-12	5.940E-14
10	5.556E+17	1.605E-12	9.617E-13	7.558E-14	6.873E-13	3.946E-15
11	3.667E+17	1.175E-12	6.587E-13	5.497E-14	4.478E-13	1.963E-15

Temp = 1300 Qrot = 7.5928 Qvib = 1.0101

		Rotational		Vibrational		
J	N(J)	I(O-branch)	I(S-branch)	I(O-branch)	I(Q-branch)	I(S-branch
0	6.886E+19	0.000E+00	2.740E-10	0.000E+00	8.768E-11	7.576E-12
1	5.417E+20	0.000E+00	1.254E-09	0.000E+00	7.186E-10	3.082E-11
2	2.299E+20	2.100E-10	4.461E-10	7.661E-12	3.008E-10	9.612E-12
3	6.445E+20	8.043E-10	1.142E-09	3.140E-11	8.396E-10	2.127E-11
4	1.612E+20	2.388E-10	2.712E-10	9.867E-12	2.090E-10	4.302E-12
5	3.013E+20	5.071E-10	4.920E-10	2.202E-11	3.889E-10	6.557E-12
6	5.290E+19	1.003E-10	8.554E-11	4.493E-12	6.708E-11	9.305E-13
7	7.132E+19	1.506E-10	1.156E-10	6.724E-12	9.087E-11	1.026E-12

8	9.172E+18	2.152E-11	1.506E-11	1.005E-12	1.159E-11	1.060E-13
9	9.150E+18	2.382E-11	1.536E-11	1.122E-12	1.145E 11	8.376E-14
10	8.765E+17	2.532E-12	1.517E-12	1.192E-13	1.084E-12	6.225E-15
11	6.545E+17	2.093E-12	1.176E-12	7.812E-14	7.994E-13	3.504E-15
12	4.710E+16	1.676E-13	8.829E-14	7.737E 15	5.670E-14	1.827E-16

Temp = 1400 Qrot = 8.1635 Qvib = 1.0141

		Rotational		Vibrational		
J	N(J)	I(O-branch)	I(S-branch)	I(O-branch)	I(Q-branch)	I(S-branch
0	5.924E+19	0.000E+00	2.357E-10	0.000E+00	7.543E-11	6.517E-12
1	4.705E+20	0.000E+00	1.089E-09	0.000E+00	6.241E-10	2.677E-11
2	2.035E+20	1.860E-10	3.950E-10	6.783E-12	2.664E-10	8.510E-12
3	5.874E+20	7.330E-10	1.041E-09	2.861E-11	7.652E-10	1.939E-11
4	1.526E+20	2.262E-10	2.568E-10	9.345E-12	1.980E-10	4.074E-12
5	2.994E+20	5.060E-10	4.890E-10	2.180E-11	3.865E-10	6.516E-12
6	5.570E+19	1.056E-10	9.006E-11	4.730E-12	7.146E-11	9.881E-13
7	8.032E+19	1.697E-10	1.301E-10	7.797E-12	1.023E-10	1.156E-12
8	1.116E+19	2.618E-11	1.831E-11	1.223E-12	1.409E-11	1.290E-13
9	1.214E+19	3.159E-11	2.037E-11	1.480E-12	1.510E-11	1.111E-13
10	1.280E+18	3.697E-12	2.216E-12	1.741E 13	1.583E-12	9.090E-15
11	1.062E+18	3.405E-12	1.907E-12	1.593E-13	1.290E-12	5.689E-15
12	8.581E+16	3.054E-13	1.609E-13	1.410E-14	1.033E-13	3.328E 16

Temp = 1500 Qrot = 8.7347 Qvib = 1.0189

		Rotational		Vibrational		
J	N(J)	I(O-branch)	I(S-branch)	I(O-branch)	I(Q-branch)	I(S-branch
0	5.143E+19	0.000E+00	2.046E-10	0.000E+00	5.549E-11	5.650E-12
1	4.119E+20	0.000E+00	9.537E-10	0.000E+00	5.464E-10	2.344E 11
2	1.812E+20	1.656E-10	3.516E-10	6.038E-12	2.371E-10	7.576E-12
3	5.361E+20	6.670E-10	9.502E-10	2.612E-11	6.985E-10	1.770E-11
4	1.440E+20	2.135E-10	2.424E-10	8.819E-12	1.869E-10	3.845E-12
5	2.946E+20	4.978E-10	4.819E-10	2.153E-11	3.803E-10	6.411E-12
6	5.761E+19	1.092E-10	9.316E-11	4.893E-12	7.392E-11	1.022E-12
7	8.808E+19	1.860E-10	1.427E-10	8.550E-12	1.122E-10	1.267E-12
8	1.308E+19	3.068E-11	2.147E-11	1.434E-12	1.652E-11	1.512E-13
9	1.533E+19	3.992E-11	2.574E-11	1.880E-12	1.910E-11	1.404E-13
10	1.758E+18	5.077E-12	3.043E-12	2.391E-13	2.175E-12	1.248E-14
11	1.599E+18	5.126E-12	2.873E-12	2.398E-13	1.953E-12	8.563E-15
12	1.428E+17	5.081E-13	2.676E-13	2.345E-14	1.719E 13	5.537E-16
13	1.014E+17	4.011E 13	1.991E-13	1.817E-14	1.201E-13	2.688E-16

Temp = 1600 Qrot = 9.3055 Qvib = 1.0244

		Rotational		Vibrational		
J	N(J)	I(O-branch)	I(S-branch)	I(O-branch)	I(Q-branch)	I(S-branch
0	4.502E+19	0.000E+00	1.791E-10	0.000E+00	5.732E-11	4.952E-12
1	3.631E+20	0.000E+00	8.408E-10	0.000E+00	4.817E-10	2.066E-11
2	1.621E+20	1.481E-10	3.146E-10	5.402E-12	2.121E-10	6.778E-12
3	4.902E+20	6.118E-10	8.689E-10	2.388E-11	6.387E-10	1.618E-11
4	1.356E+20	2.010E-10	2.282E-10	8.303E-12	1.759E-10	3.620E-12
5	2.877E+20	4.861E-10	4.705E-10	2.102E-11	3.713E-10	6.260E-12
6	5.877E+19	1.114E-10	9.503E-11	4.971E-12	7.541E-11	1.043E-12
7	9.456E+19	1.997E-10	1.532E-10	9.180E-12	1.205E-10	1.361E 12
8	1.488E+19	3.492E-11	2.443E-11	1.632E-12	1.880E-11	1.721E-13
9	1.864E+19	4.852E-11	3.129E-11	2.285E-12	2.332E-11	1.706E-13
10	2.298E+18	6.630E-12	3.970E-12	3.127E-13	2.843E-12	1.632E-14
11	2.266E+18	7.262E-12	4.070E-12	3.397E-13	2.767E-12	1.213E-14
12	2.208E+17	7.857E 13	4.130E-13	3.627E-14	2.650E-13	8.562E-16
13	1.724E+17	6.819E-13	3.385E-13	3.089E-14	2.042E-13	4.570E-16